

RICE UNIVERSITY

**Fast Electron Spectroscopy of Enhanced  
Plasmonic Nanoantenna Resonances**

by

**Jared K. Day**

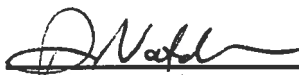
A THESIS SUBMITTED  
IN PARTIAL FULFILLMENT OF THE  
REQUIREMENTS FOR THE DEGREE

**Doctor of Philosophy**

APPROVED, THESIS COMMITTEE



Naomi J. Halas (Chair)  
Stanley C. Moore Professor of Electrical  
and Computer Engineering  
Professor of Chemistry



Douglas Natelson  
Professor of Physics and Astronomy  
Professor of Electrical and Computer  
Engineering



Peter J. Nordlander  
Professor of Physics and Astronomy  
Professor of Electrical and Computer  
Engineering



Steven J. Cox  
Professor of Computational and Applied  
Mathematics

HOUSTON, TEXAS

May 2014

# **ABSTRACT**

## **Fast Electron Spectroscopy of Enhanced Plasmonic Nanoantenna Resonances**

by

**Jared K. Day**

Surface plasmons-polaritons are elementary excitations of the collective and coherent oscillations of conduction band electrons coupled with photons at the surface of metals. Surface plasmons of metallic nanostructures can efficiently couple to light making them a new class of optical antenna that can confine and control light at nanometer scale dimensions. Nanoscale optical antennas can be used to enhance the energy transfer between nanoscale systems and freely-propagating radiation. Plasmonic nanoantennas have already been used to enhance single molecule detection, diagnose and treat cancer, harvest solar energy, create metamaterials with new optical properties, and enhance photo-chemical reactions. The applications for plasmonic nanoantennas are only limited by the fundamental understanding of their unique optical properties and the rational design of new coupled antenna systems. It is therefore necessary to interrogate and image the local electromagnetic response of nanoantenna systems to establish intuition between near-field coupling dynamics and far-field optical properties.

This thesis focuses on the characterization and enhancement of the longitudinal multipolar plasmonic resonances of Au nanorod nanoantennas. To better understand these resonances fast electron spectroscopy is used to both visualize and probe the near- and far-field properties of multipolar resonances of individual nanorods and more complex nanorod systems through cathodoluminescence (CL). CL intensity maps show

that coupled nanorod systems enhance and alter nanorod resonances away from ideal resonant behavior creating hybridized longitudinal modes that expand and relax at controllable locations along the nanorod. These measurements show that complex geometries can strengthen and alter the local density of optical states for nanoantenna designs with more functionality and better control of localized electromagnetic fields.

Finally, the electron excitations are compared to plane wave optical stimulation both experimentally and through Finite Difference Time Domain simulations to begin to develop a qualitative picture of how the local density of optical states affects the far-field optical scattering properties of plasmonic nanoantennas.

# Acknowledgments

I would like to express my sincere gratitude to everyone who has helped me during my doctoral studies at Rice University. I have the deepest admiration for the work done in the Halas Research Group and I want to thank Professor Naomi Halas for allowing me to develop as a scientist and be exposed to the many fascinating fields of science she has corralled into her portfolio. I will always appreciate her support and faith in my scientific development even in the face of experimental difficulties. I truly enjoyed experiencing the Halas Lab's creative and "daredevil" environment necessary to push scientific boundaries, as well as Prof. Halas' lead by example work ethic that challenged all students to hunt for progress every day.

I thank all of the former and current Halas group members for their help in molding me as a scientist and a person. I am especially indebted to Dr. Oara Neumann for her friendship, encouragement, and timely assistance with Chemistry! Dr. Nicolas Large fought boldly beside me as my research collaborator and simulation maestro. Thanks also to Dr. Tumasang Fofang for amazing stories I should never repeat, (but occasionally do!). It was a blast and a privilege being around the "Dell Butcher Gang" a.k.a "Chinese Mafia" and burning late night oil conducting experiments alongside with Yu Zhang, Dr. Shaunak Mukherjee, Fangfang Wen, Dr. Na Liu. I am also grateful to the senior students for helping me get adjusted initially and providing assistance or ideas for any problem: Dr. Nikolay Mirin, Dr. J. Britt Lassiter, Dr. Janardan Kundu, Dr. Nathaniel Grady. I also need to thank Lisa Brown, Dr. Alex Urban, Dr. Rizia Bardhan, Dr. Mark Knight, Andie Schlather, Ciceron Ayala-Orozco, Dr. Surbhi Lal, Nicholas King, Dr. Ryan Huschka,

Bob Zheng, Ali Sobhani, Christyn Thiboudeaux, and Dr. Sandra Bishnoi for the creativity and excitement you brought to work daily. Additionally, I was always welcomed by Dr. Natelson and his group for collaboration and idea sharing that added depth to my scientific growth at Rice. Dr. Nordlander for always having an open door and 10 more ways of looking at a situation. I am also grateful to Dr. Stephen Cox as a mentor in education outreach and piquing my interest and desiring to teach at any education level in addition to serving on my committee.

I would not have finished this work without the support of my (extended) family: Pop & Mom, (I should have visited or called more, but you loved me anyway), my sister Ryan, the Moores, Bakers, Thurstons, & Kims, Jamie McMillian, Irwin Law, R.J. Hagerman, and especially my girlfriend Jayme Yeo who has been a true partner and a firm constant on this roller coaster experience without waver.

Lastly, to my friends Harshit Chatur, Dr. Marx Mbonye, Dr. Sophia Phounsavath, Peggy Cheng, Dr. Jeremy Neill, Dr. Joe Young, Onja & Mamy-Fy (Team Madagascar), Chirag Patel, Luke Probst, Dr. Ruby Agoha, Drs. Emilia & Nissanka, the Turleys, Imaeyen Ibangi, Sertac Cakici, for always re-filling my tank.

Thank you and blessings to you all!

# Contents

<b>Acknowledgments .....</b>	<b>iv</b>
<b>Contents .....</b>	<b>vi</b>
<b>List of Figures.....</b>	<b>vii</b>
<b>Chapter 1: Introduction .....</b>	<b>1</b>
<b>Chapter 2: Optical and Electron Beam Spectroscopy of Plasmonic Nanorods .....</b>	<b>5</b>
2.1. Multipolar Optical Antennas .....	5
2.2. Optical Spectroscopy of Nanorod Resonances .....	10
2.2.1. Nanorod Fabrication .....	10
2.2.2. Dark-field Microscopy.....	13
2.2.3. Plasmon Hybridization Model .....	16
2.3. Imaging & E-beam Spectroscopy of Nanorod LDOS .....	20
2.3.1. Theory of Fast Electron Excitation of SPs .....	20
2.3.2. Experimental Imaging of Plasmonic LDOS .....	21
<b>Chapter 3: Manipulating the Characteristics of a Plasmonic Nanorod Antenna using Mode Selectors .....</b>	<b>24</b>
3.1. Introduction .....	24
3.2. Fabrication & Spectroscopy of Single Nanorod .....	26
3.3. Dual Antenna Plasmon Hybridization Model .....	30
3.4. Far-field Scattering Enhancement .....	34
3.5. CL Imaging of Dual Antenna LDOS .....	38
3.6. Modifying Nanorod LDOS .....	44
3.7. Conclusions .....	46
<b>Chapter 4: Conclusions and Future Directions.....</b>	<b>47</b>
<b>References.....</b>	<b>49</b>

# List of Figures

**Figure 2.1. Nanorod spatial charge distribution & electron amplitude distribution for multipolar plasmon modes. (A) Longitudinal and (B) transverse plasmon modes for a nanorod are identified by their respective multipolar index  $l$  and  $j$ . The ideal charge distribution for each mode is displayed on the left superimposed on a schematic of a nanorod. The electron amplitude plotted as a function of position along the nanorod is shown on the right for both (A) longitudinal and (B) transverse modes. Black arrows on the amplitude plot correspond to the direction of the electron motion and the relative dipole moment between charge accumulation sites.**

**Figure 2.2. E-beam lithography process. 1) E-beam resist, PMMA, is spin coated onto a Si wafer. 2) Patterned areas are exposed to a focused e-beam in a SEM. 3) Exposed areas are chemically removed and washed away. 4) E-beam evaporation of a thin layer of Au with a Ti adhesion layer. 5) Chemical removal of the remaining resist and metal film above it (“lift-off”), resulting in the desired patterned structure.**

**Figure 2.3. Schematics for dark-field and bright-field microscope objectives in epi-illumination configuration. Only scattered light is collected by dark-field objectives whereas both specular reflection and scattered light is collected for bright-field objectives. Modified from Söennichsen.<sup>71</sup>**

**Figure 2.4. Schematic of plasmon hybridization energy diagram for homogenous nanorod dimers. Dimer configurations of homogenous nanorods in an end-to-end or axial symmetry (AS) configuration, and in a parallel alignment, (PA), are shown with the respective hybridized modes for each configuration. Dark modes that do not radiate are indicated with a red ‘x.’ All energy scales are qualitative and relative.**

**Figure 2.5 Cathodoluminescence experimental configuration and imaging. (A) A parabolic mirror placed close to the sample is used to collect emitted photons produced by e-beam bombardment. (B) SEM image of isolated nanorod with corresponding (C) Bandwidth filtered CL photon map at 800 nm. Photon map visualizes the standing wave nature of a nanorod  $l=2$  mode. Scale bar indicates 100 nm.**

**Figure 3.1 Optical and e-beam excitation of single Au nanorod. (A) FDTD (red) and dark-field (black) scattering and CL emission spectrum (blue) of a single Au nanorod ( $420 \times 35$  nm) shows nanorod eigenmodes  $l=2-4$ . (inset) Shows expanded nanorod FDTD spectrum. Dark-field can easily excite  $l=3$  but only weakly excites**

$l=4$  through retardation effects. Both modes are more clearly observed using CL spectroscopy. (B–C) CL images of single nanorod bandpass filtered (40 nm FWHM) at (B) 650 nm and (C) 750 nm. Integrated line scans for each CL image display the standing wave nature of the nanorod resonances. (inset) SEM image of nanorod... 26

**Figure 3.2 Plasmon hybridization in a dual-antenna nanostructure. (A) Schematic of dual-antenna system: Au nanorod symmetrically positioned between two identical Au square antennas separated by gap size,  $g$ . (B) FDTD (top) and dark-field scattering (bottom) of dual-antenna system at various gap sizes,  $g$ . (C) Plasmon hybridization energy diagram of dual-antenna structure identifying spectra for isolated building blocks (blue, green, and black lines) and a fully coupled system (red line) composed of 2 side antennas (140×140 nm) and a nanorod of 420×35 nm with a gap size  $g=15$  nm. (D) Surface charge distributions associated with the primitive plasmon modes (blue, green, and black lines) and with the hybridized modes (red line) of the coupled structure. .... 30**

**Figure 3.3 Symmetric and asymmetric enhancement and activation of multipolar nanorod modes. (A) SEM images for symmetric and asymmetric nanorod (420×35 nm) configurations using Au square antennas (140×140 nm). Asymmetric geometry has square antennas longitudinally offset by  $\Delta x=140$  nm. (B) Multipolar nanorod resonances identified through CL imaging. Image borders correspond to the nanorod mode observed in each image, ( $l=3$ : purple,  $l=4$ : green,  $l=5$ : blue). Line profiles taken through the center of the nanorod are plotted below each image. (C) Scattering and CL emission spectra for dual antenna systems. Upper panel shows dark-field (black) and FDTD (red) scattering spectra. Center and lower panels display CL emission spectra and corresponding Lorentzian peak fits (hybrid-III: brown, hybrid-IV: orange, hybrid-V: gold), respectively. Color-coded vertical bars are associated with CL images in (B). Scale bars represent 100 nm..... 34**

**Figure 3.4 Spectral and imaging bandwidth of dual-antenna systems. (A) CL emission intensity spectra for dual-antenna systems with different longitudinal offsets,  $\Delta x$ , between side antennas. Dashed red lines indicate three hybrid resonances (-III, -IV, -V) for each structure. (B) Bandwidth filtered (40 nm FWHM) CL excitation maps for each dual-antenna system at different wavelengths. CL image borders are colored according to the observed nanorod mode, ( $l=3$ : purple,  $l=4$ : green,  $l=5$ : blue), determined using integrated line scans through the nanorod. .... 38**

**Figure 3.5 Mode compression/relaxation behavior for isolated nanorod and dual-antenna systems. The LSPR wavelength,  $\lambda_{sp}$ , calculated by averaging the distances between internal anti-nodes of nanorod resonances are plotted as a function of**



excitation wavelength for each system. Data points are colored according to nanorod mode excited ( $l=3$ : purple,  $l=4$ : green,  $l=5$ : blue). Dashed lines are used to highlight  $\lambda_{sp}$  trends within a given nanorod mode. .... 44

# Chapter 1

## Introduction

Nanoscience, the study of physical phenomena with nanometer size dimensions, has become a pressing topic of research among many fields of study because of the rapid advances in the control and fabrication of matter structured with nanometer precision. Nanometer sized particles lie between the molecular and macroscopic scale dimensions, giving nanostructures unique physical properties because of quantum confinement and an increased surface to volume ratio. With the advancement of better fabrication techniques, nanoparticles have been developed for *in vivo* biological probes,<sup>1-3</sup> the creation of new metamaterials,<sup>4-7</sup> wavelength-sensitive active photodetectors,<sup>8,9</sup> photocatalytic processes,<sup>10,11</sup> as well as for the study of basic science understanding of quantum processes.<sup>12-15</sup> The unprecedented imaging resolution required to interrogate nanostructures has quickly surpassed the resolution capabilities of conventional optics forcing the development of complex microscope techniques that are limited to specific configurations.<sup>16-20</sup> However, far-field optical imaging & spectroscopy is still the preferred investigative scientific tool because it is compatible with a variety of samples (e.g. *in vivo*, organic, and inorganic), environments (dry and aqueous), and is low cost and non-destructive. An alternative to developing more complex microscopy techniques is to locally enhance the absorption and emission of optical radiation below the diffraction limit of light using locally positioned optical antennas.

Optical antennas serve as transducers between free space optical radiation and localized energy of nanoscale processes just as microwave and radiowave antennas act as

transducers between electromagnetic energy and electric currents.<sup>21</sup> Placing an optical antenna near nanoscale objects can enhance Raman scattering,<sup>22,23</sup> magnify,<sup>24</sup> quench,<sup>25</sup> and control fluorescence emission,<sup>25,26</sup> provide single molecule detection,<sup>27-30</sup> re-direct optical emission,<sup>31</sup> or even acts as a thermal lens to heat cancerous cells.<sup>1,3</sup> Antennas for light have been made from silicon nanowires,<sup>32</sup> carbon nanotubes,<sup>33</sup> as well as by exploiting the plasma resonances of noble metal nanoparticles.<sup>34-37</sup> In this thesis I focus on the antenna properties of Au nanoparticles or nanoantennas, whose electronic resonances allow them to efficiently couple to light.<sup>38</sup> With improvements in fabrication plasmonic nanoantennas have become wide-spread tools in numerous research fields<sup>39-41</sup> making them ideal devices for controlling light at the nanoscale.

Surface plasmon-polaritons, SPPs, are the collective oscillations of nearly-free conduction electrons at the surface of a metal coupled to an incident electromagnetic field. These SPPs are electromagnetic modes that oscillate on the surface of a metal at the interface with a dielectric medium. Reducing the size of plasmonic metals to nanoscale dimensions allows for their plasmonic resonances to be directly excited by incident light. For nanometer sized plasmonic particles the resonant modes are referred to as localized surface plasmon modes (LSP), in contrast with propagating plasmon waves on macroscopic structures. Nanometer sized plasmonic antennas can support optically-active electromagnetic dipolar and other higher-order resonances by controlling the size, shape, local dielectric environment, and near-field coupling effects to other plasmonic antennas and nearby objects. Plasmonic resonant nanoparticles have high scattering and absorption cross sections<sup>38</sup> providing near-field enhancement capable of augmenting closely coupled weak optical processes of adjacent objects.

Traditionally scientists and optical engineers have controlled light by mimicking the design of the eye and have used lenses, mirrors, and fibers to focus, direct, and navigate light. Plasmonic nanoparticles offer a new way to focus and control light below the diffraction limit of conventional optics. Nanorods, nanometer sized cylinders or wires made of noble metals, are optical resonators that can support a number of sinusoidal plasmon resonances. Nanorods can be used as both single frequency or multi-frequency antennas. Nanorods used as a multi-functional antenna and can be used with other single mode plasmonic antennas, (disks, colloids),<sup>42</sup> and plasmonic waveguides,<sup>43,44</sup> to develop a full suite of sub-wavelength optical circuitry that can capture, direct, and emit light beyond the limits of traditional optics.<sup>45</sup>

In this thesis I have investigated the optical properties of plasmonic nanorods, high aspect ratio Au wires, to better understand their use as optical antennas. I investigated isolated and coupled nanorod geometries using both optical and cathodoluminescence far-field spectroscopy. I used the plasmon hybridization theoretical model to analytically describe the coupling mechanics of more complex designs.

Chapter 2 gives foundational information for understanding plasmonic resonances of nanorods and the experimental and theoretical techniques used to analyze these nanoantennas throughout this thesis. First, an overview of analytical and simulation techniques are described to model Au nanorod resonances. Next, the experimental fabrication and optical spectroscopy are described for single nanorod measurements. Additionally, plasmon hybridization theory is explained and used to describe a coupled nanorod system. Lastly, a background of cathodoluminescence spectroscopy and imaging is described for nanorods to finalize the characterization resources used in this thesis.

Chapter 3 will discuss enhancing the scattering power of nanorod higher-order resonances in a geometry utilizing longitudinal plasmon coupling scheme with two adjacent support nanoantennas. I used both an optical and electron beam (cathodoluminescence) spectroscopy methods to identify the hybridization effects the supporting nanoantennas have on a single nanorod.

This work is concluded in chapter 4 with a summary and suggestions for possible future research directions based on this thesis.

## Chapter 2

# Optical and Electron Beam Spectroscopy of Plasmonic Nanorods

### 2.1. Multipolar Optical Antennas

The optical properties of plasmonic metallic nanoparticles represent an important subset of light-matter interactions because the localized surface plasmon resonances offer controllable confinement of light only surpassed by molecular and atomic optical systems. The nanoparticle resonances also have enhanced electric fields within the local vicinity of the nanoparticle allowing for the enhancement of weak optical processes within the near-field of the nanoparticle. Due to their size and ability to controllably interact with light plasmonic nanoparticles can be viewed as “artificial molecules”<sup>46</sup> or nanoscale optical antennas.<sup>21,34,47</sup>

For very small spherical plasmonic nanoparticles the dipole moment, or first order electromagnetic mode, of the plasmonic resonance dominates the optical properties of the particle.<sup>35</sup> Larger spherical particles can excite strong multipolar resonant modes once phase retardation is taken in account. Retardation causes different areas of the particle to simultaneously experience different phases of the oscillating electric field activating higher-order plasmon modes. Understanding the multipolar electromagnetic modes of plasmonic antennas is important because the higher-order modes have different electric field distributions<sup>48</sup> which control the optimal location for near-field coupling<sup>49</sup> to other antennas and objects. Multipolar resonances also oscillate at different frequencies and

radiate at different emission angles<sup>38</sup> making it essential to understand and visualize these modes for new applications as well as for basic scientific understanding of how to manipulate light below the diffraction limit.

Nanorods are an important type of nanoantenna because of their potential as both sub-wavelength optical waveguides and as multi-frequency optical antennas.<sup>42</sup> The high aspect ratio between the length and base of nanorods gives them the ability to support multipolar resonances. The nanorod has two principle resonant axes; one along the length of the nanorod and a shorter one across face of its base. For nanorods with a very thin base, the shorter principle axis supports only a single transverse first-order dipolar resonance, while the longer axis contains longitudinal modes capable of supporting higher-order resonances with increasing aspect ratio. In this thesis I focus primarily on the description of the multipolar longitudinal modes along the length of the nanorod because similar first order dipolar modes have been well documented for colloids and spheroids.<sup>38,50,51</sup>

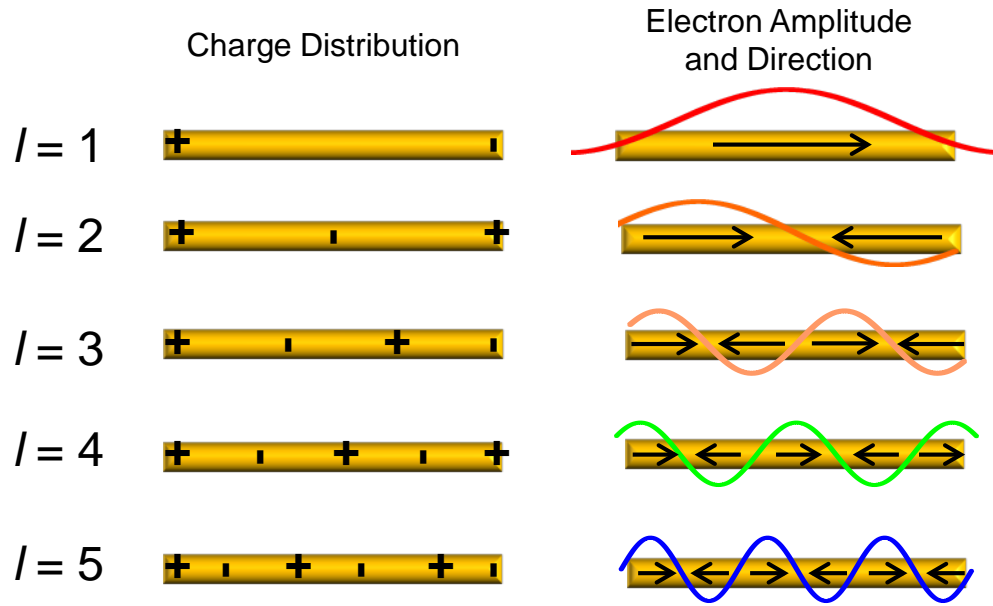
Researchers can model individual plasmonic Au nanorods as 1-D Fabry-Pérot resonators<sup>48,52</sup> and approximate the plasmonic response of Au nanorods to an illuminating optical field polarized to the nanorod length by assuming a current distribution consisting of the superposition of three harmonically oscillating currents. The nanorod current distribution consists of two counter-propagating plasmonic current waves, each with wave vector  $k_{SP}$ , superimposed with a forced current wave from the illuminating field parallel to the nanorod length.<sup>53-55</sup> This idealized current model can be used to directly calculate the scattered E-field outside the nanorod<sup>53,55</sup> or used in the 1-D Helmholtz wave

equation for an analytical solution of the surface plasmon oscillations at the nanorod surface.<sup>54</sup>

Several observations can be gleamed from these 1-D cavity models. First, by imposing that charge motion is zero at the rod end facets, the two counter-propagating harmonically oscillating plasmon waves interfere together creating standing wave resonances with  $k_{SP} L = l \pi$  and  $l$  being a positive integer index and  $L$  being the length of the nanorod. The standing wave interference dominates the forced wave term from the illuminating field.<sup>54</sup> The standing wave index number for the nanorod not only corresponds to the number of nodes in the spatial charge distribution, and the number of anti-nodes in the electron oscillation amplitude, but is also indicative of the number of dipole moments along the nanorod as shown in Figure 2.1. The index number efficiently describes the harmonic oscillation of the plasmon standing wave and is therefore used as the mode assignment number,  $l$ , for the multipolar LSP modes of the nanorod.<sup>52,56</sup>



## (A) Longitudinal Modes



## (B) Transverse Modes

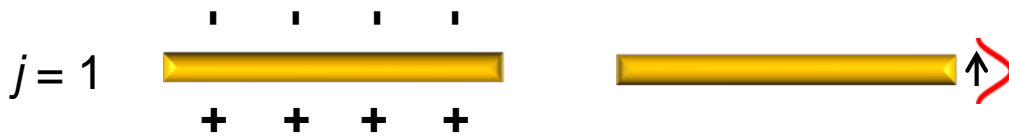


**Figure 2.1.** Nanorod spatial charge distribution & electron amplitude distribution for multipolar plasmon modes. (A) Longitudinal and (B) transverse plasmon modes for a nanorod are identified by their respective multipolar index  $l$  and  $j$ . The ideal charge distribution for each mode is displayed on the left superimposed on a schematic of a nanorod. The electron amplitude plotted as a function of position along the nanorod is shown on the right for both (A) longitudinal and (B) transverse modes. Black arrows on the amplitude plot correspond to the direction of the electron motion and the relative dipole moment between charge accumulation sites.

The quantity and magnitude of the dipole moments of a given nanorod LSP provides an intuitive understanding of the radiative strength of that mode. Ideally, the dipole moments along the nanorod are equally spaced and commensurate in magnitude.

Any two adjacent dipole moments are pointed in opposite directions along the nanorod and cancel out leaving only odd  $l$  modes with a net positive dipole moment.<sup>57</sup> For an odd- $l$  mode there is always a net positive dipole moment allowing these modes to be radiative (bright) modes. For even- $l$  modes there is a net zero dipole moment, and these modes are typically non-radiative (dark). Only through an asymmetrical activation of the various dipole moments typical of a high incident angle illumination can even- $l$  modes become radiative.<sup>52</sup> For increasing mode number the number of anti-nodes increases while the strength of the individual dipole moments along the nanorod decreases. This significantly reduces the radiative strength of both even and odd higher-order modes compared to the first order dipolar mode.

These cavity models give us an initial grasp at an intuitive understanding of the plasmonic modes of isolated nanorods but the termination points at either end of the nanorod continue to be an open problem for 1-D cavity models. At resonance the nanorod plasmon resonance creates a longitudinal and transversal E-field that extends beyond the nanorod creating a larger optical cross section than its physical dimensions; a property common to plasmonic nanoparticles.<sup>38</sup> This is especially noteworthy at the ends of the nanorod where end reflections of the current waves pick up an additional phase because of the extension of the electromagnetic fields into the surrounding medium.<sup>55,58</sup> To account for this parasitic reactance, analytical cavity models must artificially either include an additional phase shift upon reflection<sup>53</sup> or use an extended nanorod length.<sup>55,58</sup> Additionally, charge accumulates at the end of the nanorods during resonance leading to increased radiative damping.<sup>55</sup> To more accurately model multipolar nanorods, both radiative and ohmic damping, in addition to end facet reactance should be incorporated.

Analytical models provide great intuitive understanding about the underlying physical properties for plasmonic systems however, numerical simulations remain necessary to model more complex geometries. Recent advancements in numerical simulations using the Finite Element Method (FEM)<sup>59</sup> or Finite Difference Time Domain (FDTD)<sup>60</sup> techniques can calculate the electrodynamic response of most arbitrary structures. A full solution to any geometry can be found by discretizing the geometry into smaller sub-units and merging the solutions of Maxwell's equations for each sub-unit together computationally. Numerical simulations are a tremendous assistance when bridging analytical discrepancies with real world measurements. For instance the shape and curvature of nanorod ends can significantly alter the agreement between measurement and modelling.<sup>61</sup> While analytical models are important conceptualization tools for rational design of new plasmonic constructs, numerical simulations are a complementary tool used to understand deviations from ideal models that occur in normal fabrication of nanoscale structures.

## **2.2. Optical Spectroscopy of Nanorod Resonances**

### **2.2.1. Nanorod Fabrication**

Nanorods, and nanorod assemblies in general can be fabricated with a variety of methods including seed-mediated growth wet chemical techniques,<sup>62-64</sup> molecular self-assembly,<sup>65</sup> and lithographic techniques: colloidal,<sup>66</sup> scanning probe,<sup>67</sup> and electron beam (e-beam) lithography.<sup>68</sup> Chemical techniques allow for the fabrication of large amounts of nanorods, but are plagued with an unknown amount of inhomogeneity within the batch that is non-negligible. In addition to particle to particle variation aggregation of particles

within a solution also distorts and broadens the plasmon resonances making ensemble measurements difficult to correlate to single particle models and simulations. For better control of nanorod fabrication I used e-beam lithography because it offers nanometer scale control of the shape, size and precise placement of individual nanoparticles with high reproducibility. Most importantly, e-beam lithography allows for the fabrication of isolated nanorods so that spectroscopic measurements can be done at the single particle level avoiding distortions from ensemble measurements.

E-beam lithography is a mask-less lithographic technique with a pattern resolution around 15 nm. To fabricate nanorods with e-beam lithography an electron beam sensitive polymer resist (Poly(methyl methacrylate) - PMMA) is first spun on a flat substrate insuring a flat & uniform layer at the center of the substrate. I used thermally oxidized Si wafers substrates that were chemically polished to insure minimal substrate roughness. Substrates were cleaned by rinsing with acetone and isopropyl-2 (IPA), while drying substrates with N<sub>2</sub> gas between each rinse. After the resist is spin-coated onto the substrate the sample was heated on a hot plate at 180° C for 90 seconds to evaporate the solvent from the resist and to allow it to harden more quickly. Exposing the resist to a high energy and tightly focused electron beam inside a scanning electron microscope, (SEM), causes the scission of the molecular bonds allowing them to be dissolved more easily than non-exposed areas.<sup>69</sup> I used a CAD-based patterning and alignment software to control the e-beam placement & exposure dosage across the sample. After exposure the resist is soaked in a standard weak developer solution, MIBK:IPA 1: 3 (Methyl isobutyl ketone : isopropyl), for 40 seconds to remove the exposed areas. After drying, metal for the pattern is deposited with an e-beam evaporation system with a thin 2 nm Ti

adhesion layer deposited before the desired thickness of the Au layer. Finally the sample is soaked in a stronger solvent, (acetone or N-methyl-2-pyrrolidone - NMP), at temperatures up to 65° C in order to chemically remove the rest of the e-beam resist from non-exposed areas. As the remaining unexposed resist is chemically removed it also removes the metal deposited above it leaving behind metal in only the patterned areas. Nanorods fabricated using e-beam lithography are poly-crystalline giving rise to more surface roughness than chemically fabricated nanorods.<sup>70</sup> This can create significant loss for long range or guided modes but does not greatly affect the peak positions for localized transverse and longitudinal plasmon modes.

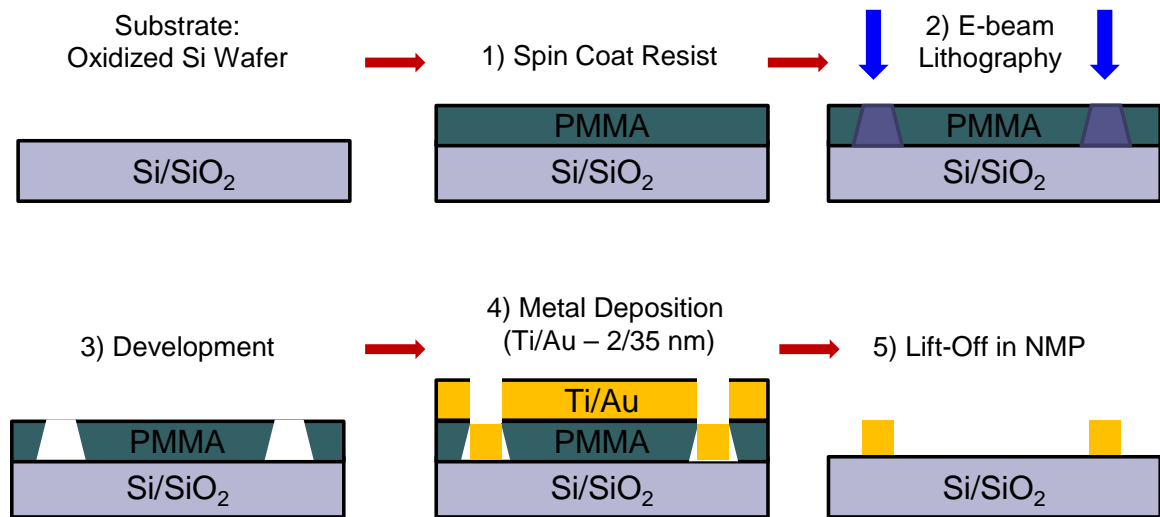


**Figure 2.2.** E-beam lithography process. 1) E-beam resist, PMMA, is spin coated onto a Si wafer. 2) Patterned areas are exposed to a focused e-beam in a SEM. 3) Exposed areas are chemically removed and washed away. 4) E-beam evaporation of a thin layer of Au with a Ti adhesion layer. 5) Chemical removal of the remaining resist and metal film above it (“lift-off”), resulting in the desired patterned structure.

To ensure that spectra of different nanostructures were isolated, nanostructures were fabricated with a separation distance of at least 10 square microns.

### **2.2.2. Dark-field Microscopy**

Optical spectroscopy is an ideal measurement tool for investigating the plasmonic resonances of noble metal nanoparticles because their plasmon resonances are located at discrete wavelengths and ideally transparent to light at all other wavelengths giving them a unique spectroscopic signature. To obtain spectra from individual nanorods I used a dark-field microscope that allowed for the isolation and sensitivity necessary for single particle measurements.

Dark-field microscopy is widely used to investigate the optical properties of plasmonic antennas because of its simple optical design, its ability to measure samples in ambient air or in solution, and most importantly its sensitivity to scattering from isolated individual nanostructures by eliminating the incident illumination from the collecting optics. A dark-field microscope is used to image and collect light from a nanostructure, which can then be routed to a spectrometer for analysis. The optics of the dark-field microscope will be described below.

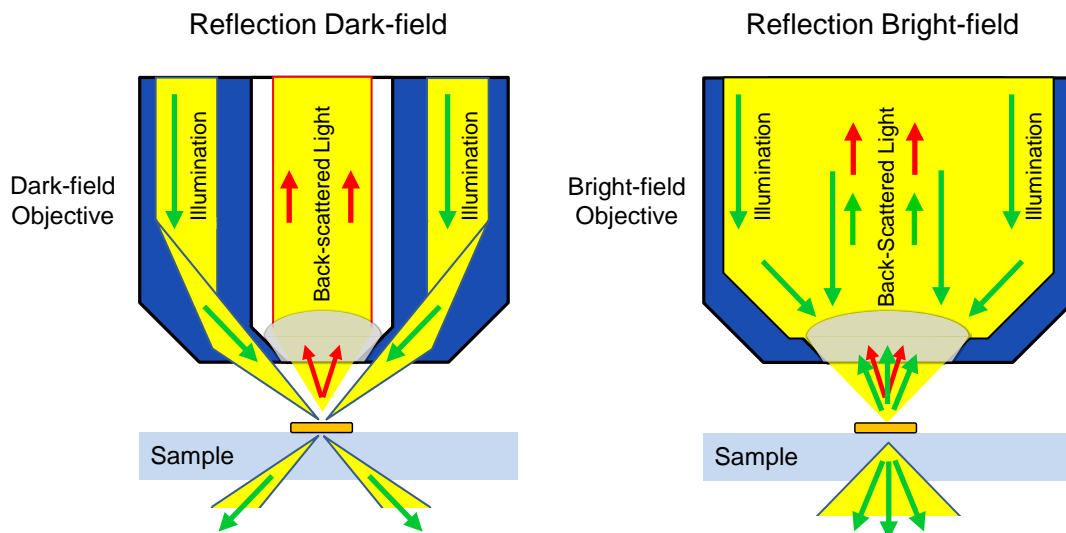


**Figure 2.3.** Schematics for dark-field and bright-field microscope objectives in epi-illumination configuration. Only scattered light is collected by dark-field objectives where as both specular reflection and scattered light is collected for bright-field objectives. Modified from Söennichsen.<sup>71</sup>

Dark-field microscopy is a technique that collects only the scattered light of the sample into the objective solid angle while omitting the rest of the incident illumination.<sup>72</sup> The illumination source is directed toward the sample at an incident angle higher than the solid angle of the collection objective with respect to the sample normal. This prohibits both the incident and the reflected light of the direct illumination from being captured by the objective and only the scattered light from the nanostructure is captured. Images captured by dark-field microscopes resemble pictures of stars at night; they have a characteristically dark background with light scattered only at individual scattering points in the image. This contrasts with typical bright-field microscopes that produce dark spots on a bright background because the incident light is reflected or transmitted back into the

objective with the light absorbed or scattered from individual points is removed from the image.

Dark field microscopes were originally developed by Richard Zsigmondy in the early 20<sup>th</sup> century and were referred to at the time as ultramicroscopes because of their ability to analyze the scattered light from individual nanoparticle colloids in suspension.<sup>72</sup> Dark field microscopes are also extensively used in biological studies of blood cells<sup>73</sup> and have inspired other microscope designs with characteristic dark backgrounds such as total internal reflection spectroscopy.<sup>74</sup>

The optical spectra recorded in this thesis used a commercial microscope in a reflection dark-field configuration. The illumination source and the collecting objective share the same optical path but the illumination is steered through optics in the outer portion of the objective housing separated from the collection optics housed in the objective interior (Figure 2.3). The scattered light collected into the objective was then sent to a spectrometer for analysis.

For polarization dependent measurements an analyzer was placed into the optical path after the collection optics and before the spectrometer. When using an un-polarized illumination source all plasmon modes of the nanostructure were excited and the analyzer selected only the modes aligned along its polarization direction. Polarization measurements were used to separate transverse and longitudinal coupling interactions by aligning the analyzer along either the longitudinal or transverse axis of the nanostructure. This polarization method works best for plasmon oscillations parallel to the substrate.



### 2.2.3. Plasmon Hybridization Model

The plasmon resonance of metallic nanoparticles depends not only on particle geometry, size and material composition but is crucially affected by near-field coupling to neighboring objects and other plasmonic particles. Advances in the understanding of nanoparticle coupling interactions have led to increased understanding of optical antenna design at the nanoscale including nanostructures such as nanoshells,<sup>37</sup> nanomatrushkas,<sup>75</sup> split-ring resonators,<sup>76,77</sup> and bow tie antennas.<sup>78,79</sup> Numerical simulations can calculate the electromagnetic scattering and absorption of different antenna designs but do not always provide intuition into how the separate plasmonic units interact together making it difficult to improve designs. For more intuition on the behavior of coupled antenna geometries I used plasmon hybridization theory<sup>37</sup> to better understand new antenna designs.

The plasmon hybridization model is a nanoscale analytical electromagnetic model that describes complex plasmonic geometries as the cumulative interaction between simple constituent plasmon modes within the collective structure.<sup>37,80,81</sup> This model is an electromagnetic analogy to molecular orbital theory that predicts how atomic orbitals interact to form more complex molecular orbitals.<sup>46</sup> For two identical interacting nanorods, (homogeneous nanorod dimers), plasmon hybridization shows how the individual longitudinal and transverse modes of a single nanorod hybridizes with the plasmon modes in the second nanorod to form bonding (attractive) and anti-bonding (repulsive) modes controlled by the incident polarization, particle orientation angle, and separation distance.<sup>82,83</sup> The energy of the resultant hybrid modes can be tuned by changing the interaction strength between the two nanorods.

Unlike spherical dimers, nanorod dimers can be positioned in a number of different arrangements resulting in various plasmon coupling interactions dependent on the respective strength of coupling. Plasmon hybridization theory is used to interpret and illustrate the longitudinal plasmon coupling between dipole moments of two homogenous nanorods (Figure 2.4). By only considering incident light polarized parallel to the nanorod length we can selectively isolate the longitudinal modes of the nanorod. In Figure 2.4, the hybridization energy diagram for nanorod dimers is confined to represent only the longitudinal-longitudinal plasmon interactions as analogous arguments can be made for transverse-transverse interactions. The relative energy diagram is a qualitative representation of hybridization calculations that increases in energy from the bottom to the top of Figure 2.4.

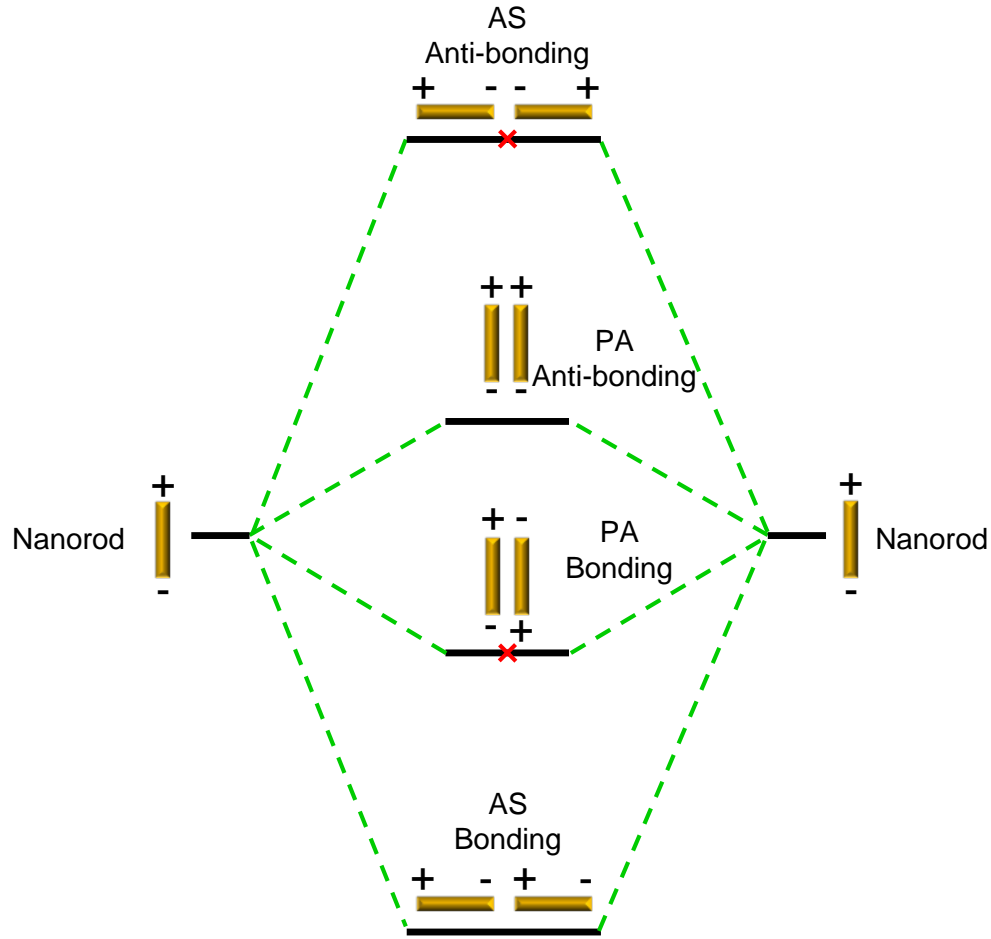


**Figure 2.4.** Schematic of plasmon hybridization energy diagram for homogenous nanorod dimers. Dimer configurations of homogenous nanorods in an end-to-end or axial symmetry (AS) configuration, and in a parallel alignment, (PA), are shown with the respective hybridized modes for each configuration. Dark modes that do not radiate are indicated with a red 'x.' All energy scales are qualitative and relative.

The two identical nanorods start with the same plasmon energy level when they are separated by a large distance ( $\geq 200$  nm) and therefore are only very weakly interacting. Figure 2.4 shows low aspect ratio nanorods where only the  $l=1$  dipole mode is shown for each nanorod. For nanorods in an axially symmetric (AS), end-to-end dimer configuration that exhibit cylindrical symmetry a polarization along the dimer axis

creates an energy splitting of the coupled  $l=1$  nanorod modes into a high-energy AS anti-bonding mode and a low-energy AS bonding mode. The high energy AS anti-bonding mode consists of the two dipole moments opposed to each other in an anti-symmetric configuration that results in a net zero total dipole moment. Without an effective dipole moment the anti-bonding mode cannot efficiently couple to light making it optically inactive and commonly referred to as a “dark mode.” The lower energy AS bonding mode has a symmetric or attractive alignment of the dipole moments which results in lower energy compared to the individual nanorod mode with a corresponding red-shift in wavelength resonance with respect to the energy level of an isolated nanorod.

For nanorod dimers in a parallel alignment (PA), incident light polarized aligned perpendicular to the dimer axis creates charge distributions for the bonding and anti-bonding hybridized modes are reversed to the AS configuration.<sup>83</sup> The PA bonding mode is higher energy with symmetric charge alignment which blue shifts with decreasing separation distance while the PA anti-bonding mode is the lower energy dark mode with an anti-symmetric alignment which red-shifts with decreasing separation distance.

Although the overall energy splitting and therefore the coupling strength is reduced in the PA when compared to the AS configuration, the larger lateral width of the junction and the lack of azimuthal symmetry in PA allows for more interaction between the optically active  $l=1$  modes and with the higher order modes (not shown) in the adjacent nanorod.<sup>83</sup> This admixture between the optically active dipole modes and weakly scattering multipolar modes results in a larger number of higher order modes that are optically active for nanorod dimers aligned in parallel than for the AS end-to-end configuration.

The work in this thesis is primarily concerned with the activation of longitudinal plasmon modes making the parallel alignment between adjacent nanorods the most applicable configuration. Other dimer coupling arrangements consisting of nanorod dimers have been studied to better understand the coupling dynamics in more complex orientations often found in nanoparticle ensembles which including dimers at right angles in L- and T- configurations<sup>84</sup> and arbitrary of angular offsets between nanorods.<sup>82</sup>

## **2.3. Imaging & E-beam Spectroscopy of Nanorod LDOS**

### **2.3.1. Theory of Fast Electron Excitation of SPs**

Although SPPs are typically excited with optical sources whose electric fields oscillate at frequencies high enough to excite plasmonic resonances, fast electrons can also excite SPPs as was shown in pioneering work from the 1950s on electron beam bombardment of thin films that led to the initial discovery of SPPs.<sup>85-88</sup> When measuring the inelastic interaction of electrons with thin metallic films the resultant electron energy distribution showed loss mechanisms attributed to SPP modes in the metal. Researchers have recently revisited the idea of using fast electrons to excite SPPs due to the advancement of electron beam microscopy technology. With a smaller de Broglie wavelength than a photon tightly focused electrons ( $\sim 5 \text{ nm}^{68,89}$ ) provide a localized SP excitation source capable of resolving plasmons spectrally and spatially beyond the resolution limitation of conventional optics.

Qualitatively, when an electron makes impact with a metal it creates a local perturbation of the conduction electrons. The incoming charge of the electron combined

with its image charge in the metal behaves like an electric dipole. This transient electric dipole together with the local perturbation emits radiation, via transition (TR) or Cherenkov radiation (CR), and excites SPPs in a metal.<sup>89-91</sup> The resulting interaction of the electron with the metal can be determined either by measuring the energy loss of the electron as it passes through the sample, (electron energy loss spectroscopy), or by measuring the radiative energy produced from the combination of TR, CR as well as and plasmon decay into far-field radiation (cathodoluminescence). Electron energy loss spectroscopy (EELS) allows for the detection of all plasmon modes both radiative (bright) & non-radiative (dark) but only works for thin samples in a transmission electron microscope (TEM).<sup>89,92</sup> In Cathodoluminescence (CL) spectroscopy (Figure 2.5A), detection is limited to the radiative modes of a sample coupled to the density of optical states of the impact site, but is able to resolve the angular emission profile of these modes and polarization of the emitted photons which cannot be measured in EELS.<sup>57,90,93</sup> Also, CL is measured above the sample instead of below it as in EELS systems allowing CL spectroscopy to be placed into more commonly available SEM systems. Although CL and EELS are complementary techniques I focused on CL spectroscopy in this work because of the advantages in observing the radiative modes of plasmonic nanoparticles.

### **2.3.2. Experimental Imaging of Plasmonic LDOS**

Applying the same qualitative picture for the interaction between an electron and a plasmonic antenna to produce a transient electric dipole at the point of impact, the power emitted by the transient dipole is related to local density of plasmonic states with a given relation:

$$P = \frac{\pi\omega^2}{12\varepsilon_0} |\mathbf{p}|^2 \rho_{\mathbf{p}}(\mathbf{r}, \omega) \quad (1)$$

where  $\mathbf{p}$  is the transient or induced dipole for CL, and  $\rho_{\mathbf{p}}$  is the radiative portion of the local density of states (LDOS) projected along the direction of the transition dipole.<sup>47,94</sup> This simple analytic expression conveys that the radiative power of the transient dipole efficiently couples through the radiative modes of antenna into the far-field. Since the LDOS of plasmonic antennas which are very strongly correlated to the electric field of the plasmon modes of an antenna,<sup>95-97</sup> scanning the electron beam across the entire nanoantenna allows us to spectrally resolve radiative modes of individual nanoantennas with a localized source.

By scanning the e-beam over a nanoantenna and associating the photon intensity with the scan position a photon excitation map can be created indicating the optical resonance of the antenna with nanoscale resolution ( $\sim 5$  nm). Each pixel is the superposition of the radiative strength of all plasmon modes of the nanostructure, both directly connected and coupled, at the scan location. This means that the serial e-beam scanning of the nanostructure excites a weighted response of all of the plasmon modes dependent on beam position. For a given excitation point the CL intensity is collected both from modes directly excited through direct physical contact with the scan location or for complex geometries with separation between nanostructures from induced modes that are activated through the near-field coupling from directly excited modes. By polarizing or wavelength filtering the collected photons we can map individual plasmon modes with position dependent CL intensity. These plasmon maps, as seen in Figure 2.5C, represent a

purely unperturbed visualization of the radiative portion of the LDOS unlike near-field tip probe techniques whose proximity directly alters the EM-LDOS.

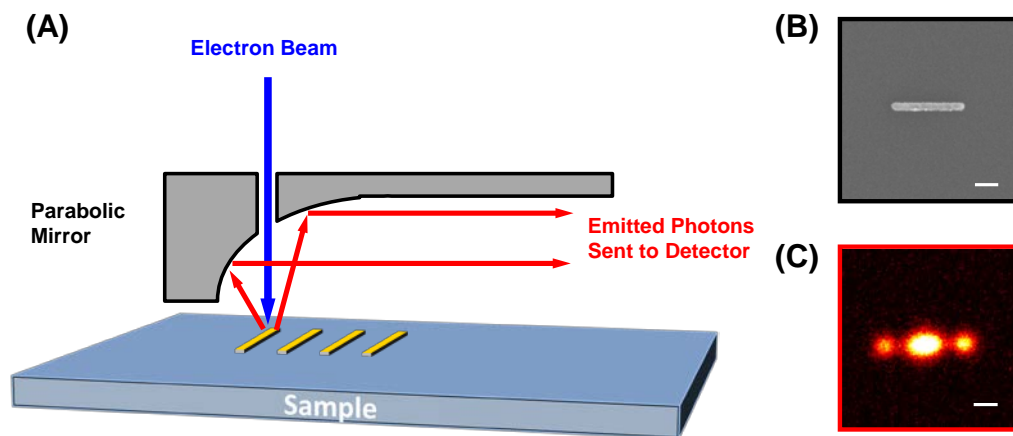


**Figure 2.5** Cathodoluminescence experimental configuration and imaging. (A) A parabolic mirror placed close to the sample is used to collect emitted photons produced by e-beam bombardment. (B) SEM image of isolated nanorod with corresponding (C) Bandwidth filtered CL photon map at 800 nm. Photon map visualizes the standing wave nature of a nanorod  $l=2$  mode. Scale bar indicates 100 nm.



# Chapter 3

## Manipulating the Characteristics of a Plasmonic Nanorod Antenna using Mode Selectors

### 3.1. Introduction

Optical nanoantennas serve as conduits between nanoscale optical phenomena and free-space optical radiation.<sup>21</sup> Plasmonic nanorods, high aspect ratio nanoantennas, have gained significant interest because of their ability to enhance emission from quantum emitters,<sup>29</sup> serve as antenna receivers for ultrasensitive sensing applications,<sup>98,99</sup> and single molecule detection,<sup>30,98</sup> in addition to becoming an elementary unit for a new generation of sub-wavelength opto-electronic devices.<sup>45,49,100,101</sup>

Nanorods are an essential building block for future nanophotonic design because of their ease of fabrication<sup>62-64,68,102</sup> and their simple analytical description. These nanoantennas support multipolar longitudinal localized surface plasmon resonances (LSPRs) in the form of plasmon standing waves that can be well described by 1-D damped Fabry-Pérot cavity models.<sup>53-55,58,103,104</sup> These 1-D plasmon standing waves can be identified by the positive integer mode index,  $l$ , for the standing wave geometric condition:  $l \times (\lambda_{sp}/2) = L$ , where  $\lambda_{sp}$  is the surface plasmon wavelength, and  $L$  is the length of the optical cavity (i.e. nanorod).<sup>52,105</sup> However, full far-field accessibility of higher-order LSPRs is limited by their weak interaction with light caused by the increasingly small net dipole moment of each higher-order mode.<sup>106</sup> In practice, nanorod

LSPRs have been increasingly investigated for their optical technological potential<sup>105,107,108</sup> but only the dipolar resonances (both longitudinal and transverse) are utilized in most applications.<sup>102,109,110</sup> Multipolar nanorod resonances can become optically active through retardation due to increasing nanorod size<sup>106</sup> but different incident angles are still needed to excite symmetry restricted even-order modes.<sup>52</sup>

Nanorods could be used as more effective multi-modal optical antennas by enhancing the radiative decay of higher-order modes. This enhanced functionality would provide wavelength dependent control of near-field coupling<sup>49</sup> and angular emission<sup>93,111</sup> due to the unique spatial and scattering characteristics of each mode.<sup>57</sup> The scattering power of nanorod LSPRs can be enhanced by hybridizing nanorods with stronger dipole scatterers.<sup>83,112</sup> While experimental understanding of isolated nanoantenna components has been well established<sup>52-54,105</sup> coupled plasmon geometries still need intuitive analytical design rules. Peak energy shifts of quasi-static hybridized nanorod geometries can be accounted for in plasmon hybridization theory,<sup>83,84,112</sup> but the spatial distribution and near-field intensity variations within more complex nanorod geometries cannot be accounted for with hybridization theory or any current analytical 1-D cavity model.

In this work, we present a simple coupled nanostructure geometry to enhance higher-order nanorod modes. Due to the newly fashioned properties and behaviors of these hybridized nanorod modes<sup>91</sup> we employ both far- and near-field measurements to characterize these new modes with both dark-field and cathodoluminescence spectroscopic techniques. We identify unique behavior through mode hybridization that introduces spatial deviations, near-field intensity variation, and unique mode transitions not seen in isolated nanorods or predicted by current analytical models.

### 3.2. Fabrication & Spectroscopy of Single Nanorod

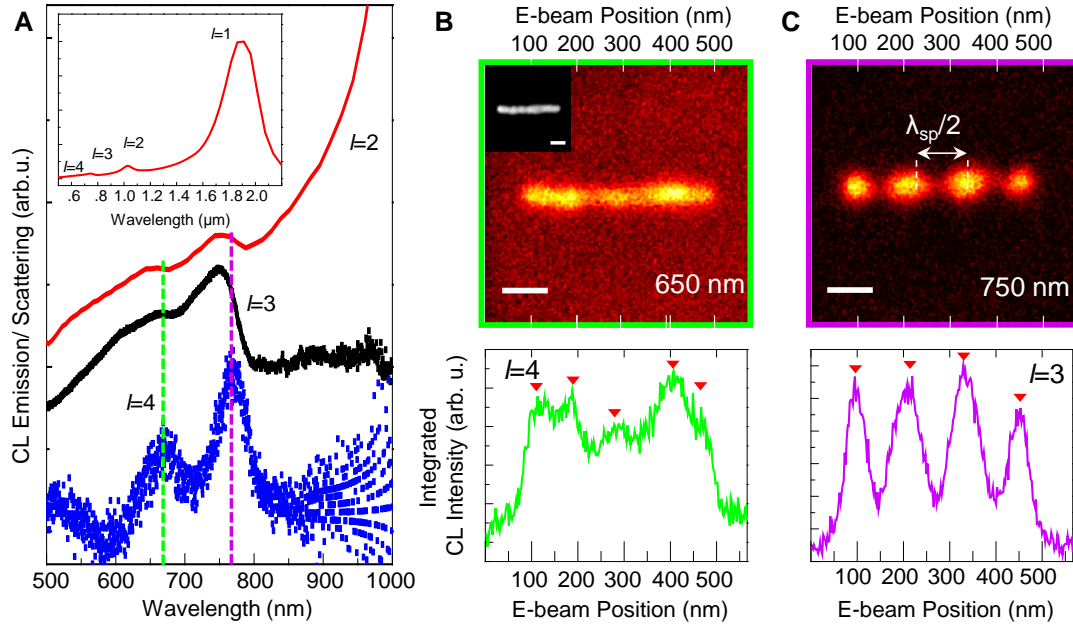


**Figure 3.1** Optical and e-beam excitation of single Au nanorod. (A) FDTD (red) and dark-field (black) scattering and CL emission spectrum (blue) of a single Au nanorod ( $420 \times 35$  nm) shows nanorod eigenmodes  $l=2-4$ . (inset) Shows expanded nanorod FDTD spectrum. Dark-field can easily excite  $l=3$  but only weakly excites  $l=4$  through retardation effects. Both modes are more clearly observed using CL spectroscopy. (B–C) CL images of single nanorod bandpass filtered (40 nm FWHM) at (B) 650 nm and (C) 750 nm. Integrated line scans for each CL image display the standing wave nature of the nanorod resonances. (inset) SEM image of nanorod.

Individual Au nanorods used in this study were fabricated by conventional electron beam (e-beam) lithography on a Si wafer with 100 nm of oxide used to isolate the nanorods from the Si substrate. 35 nm thick Au nanorods were deposited with e-beam evaporation using a thin 2 nm Ti adhesion layer. Nanorods were all fabricated with the

same surface cross-section of  $420 \times 35$  nm as our designed goal was to enhance the scattering power of multipolar modes of a single nanorod antenna without the need to vary aspect ratio or incident illumination angle to activate new modes.

Individual scattering spectra for nanorods were measured in a dark-field microscope (Figure 3.1A). Unpolarized white light from a halogen lamp was focused onto the nanorods at a high incident angle in an epi-illumination configuration in a Zeiss Imager A2 microscope (NA=0.75, Zeiss LD EC Epiplan-Neofluar 100X Objective). Scattered light was collected and passed through a linear analyzer oriented with the longitudinal axis of the nanorod before entrance into a spectrograph and CCD detector (Synapse, Jobin Yvon) for analysis. The spectrum for individual nanorods was also calculated using the finite-difference time-domain method (FDTD, Lumerical Solutions). The geometry was defined from the parameters extracted from SEM images of the nanoantennas. The 2 nm Ti adhesion layer and the SiO<sub>2</sub> substrate were also taken into account. Simulations used the bulk dielectric function tabulated by Johnson and Christy for Au<sup>113</sup> and the dielectric functions reported by Palik were used for Ti, and SiO<sub>2</sub>.<sup>114</sup> Finally, simulations were performed for an optical excitation at oblique incidence to account for the experimental configuration.

Cathodoluminescence (CL) imaging and spectroscopy was also used to examine the nanorod structures because the electron beam excitation of surface plasmon modes has no symmetry restrictions allowing all plasmon modes to be excited in a weighted plasmon response dependent on the position of the scanning electron beam. Additionally, the high spatial localization of the electron beam irradiation allows for nanoscale resolution of plasmon excitation images to be constructed that are proportional to the

radiative local density of optical states (LDOS) of the nanorods.<sup>89,97</sup> CL measurements were taken using a combined Gatan (MonoElite CL4) spectrometer, light probe, and software acquisition unit attached to a scanning electron microscope (SEM, FEI Quanta 650) chamber. A parabolic mirror (NA=0.89), containing a hole to transmit the focused high energy electron beam (30 keV) onto the sample, was placed ~200 nm above the sample and collected emitted photons into the light probe where photons were focused and sent to a detector. The collected light was then linearly polarized along the longitudinal axis of the nanorod (matching the optical dark-field configuration) and either dispersed by a grating across a CCD for spectroscopy or directed to a PMT to produce raster-scanned CL excitation images. Bandpass filters were inserted into the optical path before the PMT to create wavelength specific raster-scanned CL excitation images. Background correction for all CL spectra were performed to reduce non-plasmonic sources of radiation from substrate luminescence and transition radiation.<sup>115</sup>

The dark-field scattering spectrum for an isolated nanorod (Figure 3.1A, black line) can only resolve one fully formed nanorod resonance within our detector range (500-1000 nm) at ~760 nm with a broad shoulder at 680 nm in agreement with simulations (Figure 3.1A, red line). The CL emission spectrum for the same nanorod better resolves these optical features as two separate nanorod resonances: the  $l = 3$  and  $l = 4$  nanorod higher-order modes. The optical excitation can only weakly excite even-order modes through the off-normal incident excitation angle of the dark-field optical setup (NA=0.75) in contrast to the e-beam irradiation of CL which locally excites all nanorod modes.<sup>89</sup> This difference between the excitation geometries leads to differences

in the relative intensities between nanorod LSPRs but not a disagreement in the LSPR positions.

Bandpass filtered CL excitation images were created at the two nanorod resonances and shown in Figure 3.1B and 3.1C. The standing wave nature of the longitudinal nanorod resonances are clearly seen in the CL excitation image at 750 nm (Figure 3.1C) for the  $l = 3$  mode as expected from Fabry-Pérot cavity modes (Q~5).<sup>52,104,116</sup> Integrated line scans taken through the center of the nanorod, displayed below their corresponding excitation images, more clearly show the spatial profile of each nanorod LSP mode.

The similarities with ideal Fabry-Pérot resonances begin to break down at shorter wavelengths as the weakly excited  $l = 4$  mode near 650 nm (Figure 3.1B) shows a variation in the intensities of the anti-node sites. Previous CL and EELS reports have consistently reported higher anti-node intensities not from the end positions but from the anti-nodes next to the end positions.<sup>97,105,107,108</sup> This effect can be seen from the CL map and line scan at 650 nm (Figure 3.1B). The cause of this slight deviation of the plasmonic LDOS of the nanorod away from ideal Fabry-Pérot standing waves is thought to be due to the reflection mechanism at the nanorod ends.<sup>105</sup> However, this effect is only prominent on our measurement for the weakly excited  $l = 4$  mode. Although a completely different method of excitation, the CL spectroscopy and imaging allows us to compare, and complement the more technologically relevant far-field optical measurements.

### 3.3. Dual Antenna Plasmon Hybridization Model

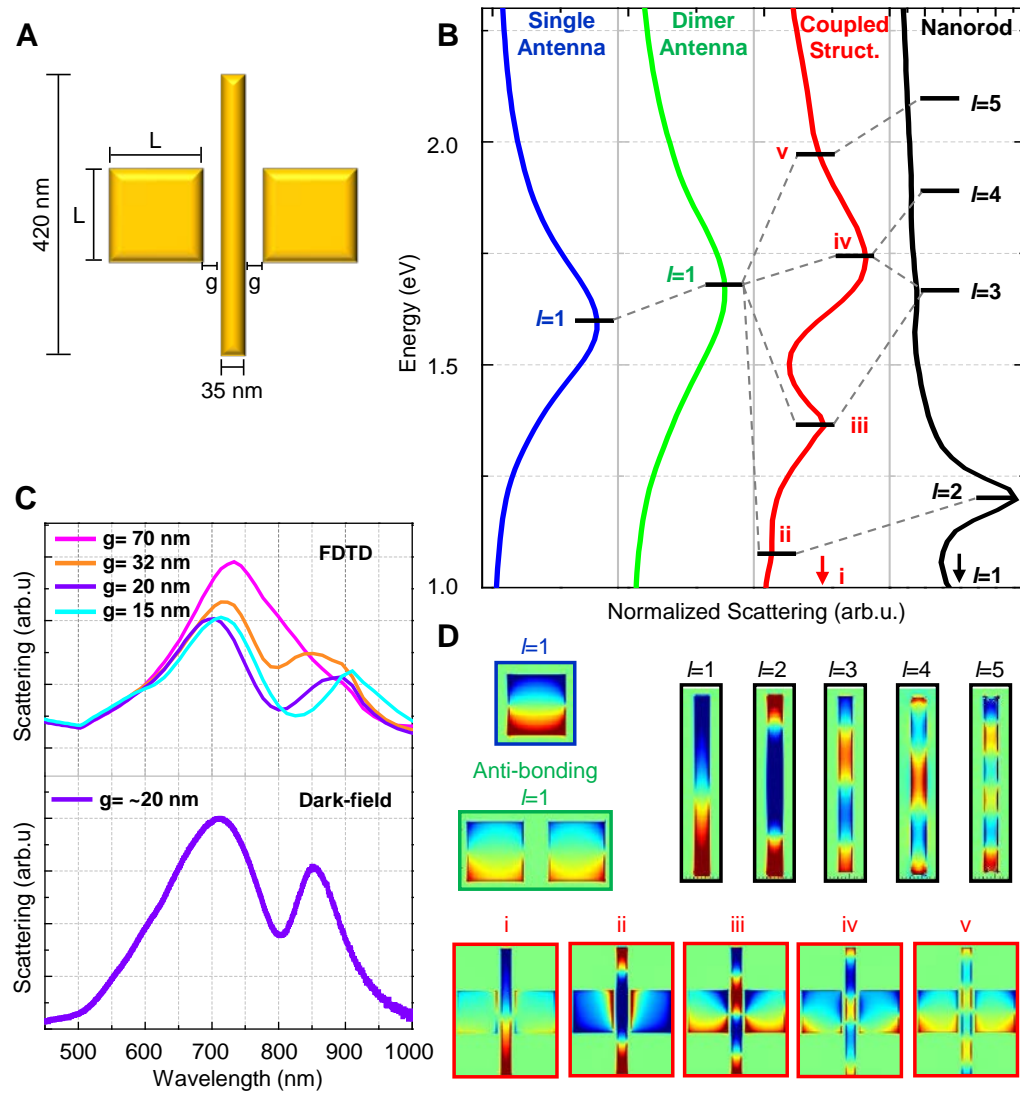


**Figure 3.2** Plasmon hybridization in a dual-antenna nanostructure. (A) Schematic of dual-antenna system: Au nanorod symmetrically positioned between two identical Au square antennas separated by gap size,  $g$ . (B) FDTD (top) and dark-field scattering (bottom) of dual-antenna system at various gap sizes,  $g$ . (C) Plasmon hybridization energy diagram of dual-antenna structure identifying spectra for isolated building blocks (blue, green, and black lines) and a fully coupled system (red line) composed of 2 side antennas (140×140 nm) and a nanorod of 420×35 nm with a gap size  $g=15$  nm. (D) Surface charge distributions associated with the primitive plasmon modes (blue, green, and black lines) and with the hybridized modes (red line) of the coupled structure.

To more easily observe scattered radiation from higher-order nanorod LSP modes without increasing nanorod size<sup>53,57,117</sup> or using increased incident particle energy<sup>105,108</sup> we enhanced the radiative scattering cross-section of these modes through near-field coupling to two identical square dipole antennas in a dual-antenna nanostructure configuration. The designed structure, pictured in Figure 3.2A, was fabricated using the same one-step e-beam lithography process used for single Au nanorods. The length of the Au square antennas was determined by matching the poles of the square antenna dipole (i.e. its length) with the ends of two adjacent anti-nodes (i.e. one wavelength) of the highest-order nanorod mode detectable by our optical detectors. We chose to enhance the scattering power of the weakly scattering  $l = 5$  mode, forcing our square antennas to be fabricated with a length of 140 nm that corresponded to the  $\lambda_{sp}$  of an ideal  $l = 5$  Fabry-Pérot resonance. Two side antennas were used to provide equal coupling to both sidewalls of the nanorod.

FDTD calculations were performed to investigate the optical spectral evolution of the dual-antenna design as a function of the gap spacing between the side antennas and the nanorod (Figure 3.2C). As gap size decreases (i.e. increasing coupling) the spectrum changes from one large peak encompassing various overlapping resonances to a scattering spectrum consisting of two well separated LSPRs at 700 and 850 nm when reaching a gap size of 15 nm. The dual-antenna nanostructure was fabricated by targeting the smallest gap configuration in order to achieve a large peak separation. The resulting coupled structure has an experimental gap size of ~20 nm. Dark-field scattering spectrum



(lower panel in Figure 3.2B) is in excellent agreement with the FDTD predictions for the 20 nm gap spacing.

The spectral features of the dual-antenna nanostructure can be better explained by plotting the plasmon hybridization energy diagram (Figure 3.2B). This hybridization diagram shows how the primitive LSP modes of the individual building blocks (side antennas and nanorod) couple to each other to form the hybridized LSP modes of the coupled nanostructure. In the absence of a center nanorod, the side antennas form a weakly coupled dimer separated by  $\sim 70$  nm (Figure 3.2B, green line). The LSPR of this dimer slightly blue-shifts from a single square antenna LSPR (Figure 3.2B, blue line) when longitudinally polarized due to anti-bonding coupling of the two attractive dipole resonances.<sup>112</sup> A single Au nanorod (Figure 3.2B, black line) has two odd-order LSP modes ( $l = 3, 5$ ) in the visible range and an even-order LSP mode ( $l = 4$ ) between them at 680 nm (1.82 eV) that scatters due to retardation effects from the off-normal incidence excitation ( $\theta_i = 48^\circ$ ). Once fabricated within the gap of the dimer, the resonance of the side antennas and the higher-order LSPRs of the nanorod hybridize. The strong interaction between the dipolar side antennas and the  $l = 3$  nanorod mode results in energy splitting of the two modes when brought in close proximity due to the close spectral alignment between the plasmon modes (Figure 3.2B, red line). This splitting gives rise to a bi-modal spectrum consisting of a narrow  $l = 3$  nanorod-dominant peak (Figure 3.2B, red line – iii) hybridized with the  $l = 1$  LSPR of the dimer side antennas (hybrid-III) at lower energy (i.e. longer wavelength), and broader peak consisting of two overlapping hybridized peaks (Figure 3.2B, red line – iv, v) at higher energy (i.e. shorter wavelength). Hybrid-IV is dominated by the dimer LSPR and is predominately

hybridized with the  $l = 3$  and  $l = 4$  nanorod modes but also with the  $l = 5$  mode to a lesser extent. The hybrid-V peak consists of an admixture of the  $l = 4$  and  $l = 5$  nanorod modes hybridized with the LSPR of the side antennas. This hybridized mode is lower in amplitude than hybrid-IV because of greater energy separation between the  $l = 5$  nanorod mode and the dimer LSPR. The charge distributions for all of the primitive and hybridized plasmon modes are shown in Figure 3.2D.

### 3.4. Far-field Scattering Enhancement

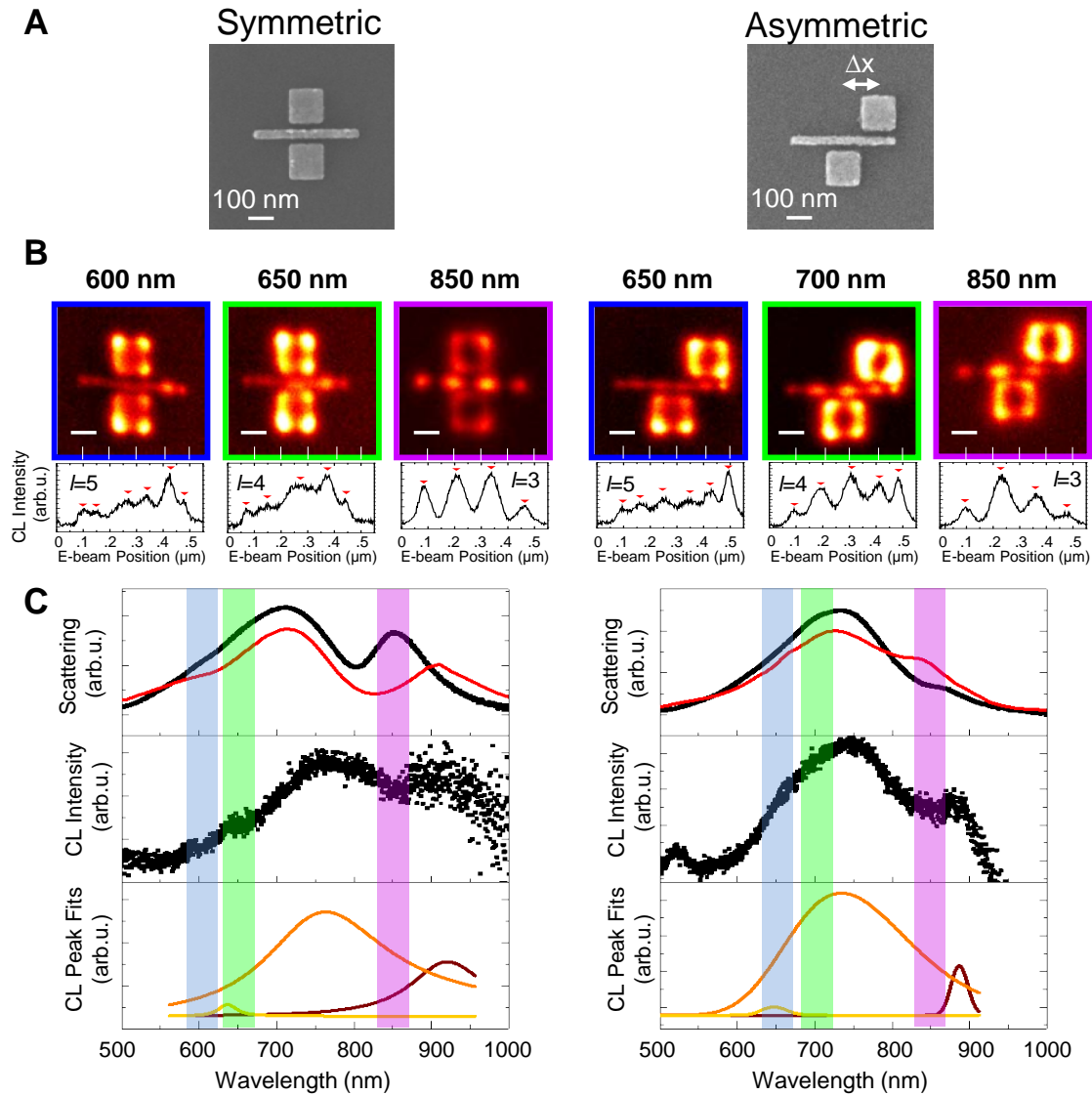


**Figure 3.3** Symmetric and asymmetric enhancement and activation of multipolar nanorod modes. (A) SEM images for symmetric and asymmetric nanorod (420×35 nm) configurations using Au square antennas (140×140 nm). Asymmetric geometry has square antennas longitudinally offset by  $\Delta x = 140$  nm. (B) Multipolar nanorod resonances identified through CL imaging. Image borders correspond to the nanorod mode observed in each image, ( $l=3$ : purple,  $l=4$ : green,  $l=5$ : blue). Line profiles taken through the center of the nanorod are plotted below each image. (C) Scattering and CL emission spectra for dual antenna systems. Upper panel shows dark-field (black) and FDTD (red) scattering

spectra. Center and lower panels display CL emission spectra and corresponding Lorentzian peak fits (hybrid-III: brown, hybrid-IV: orange, hybrid-V: gold), respectively. Color-coded vertical bars are associated with CL images in (B). Scale bars represent 100 nm.

For side antennas symmetrically positioned along both sides of the nanorod at its midpoint (Figure 3.3A, left panel), line profiles extracted from bandpass filtered CL excitation maps (Figure 3.3B, left three panels) show the observation of three distinct nanorod resonances,  $l = 3, 4, 5$  at 850, 650, and 600 nm, respectively, enhanced by hybridization with the dipolar LSP mode of the side antennas. Although hybridized with the dimer mode of the side antennas the spatial distribution of the nanorod modes still resembles a standing wave distribution at specific wavelengths. The line profile plots were scaled to align its positional axis to the dimension of its corresponding CL image. The nanorod modes are color coded and are also identified chromatically at their corresponding wavelength on the optical and CL spectra (Figure 3.3C, left panel). The width of the colored bars corresponds to the 40 nm bandwidth used to filter the CL images.

We obtain very close agreement between both scattering and CL spectra for the symmetrically aligned dual-antenna configuration (Figure 3.3, black). However, one can notice a red-shift ( $\sim 50$  nm) of the CL spectrum (Figure 3.3, center panel) in relation to the dark-field spectrum (Figure 3.3, upper panel) that can be attributed to the gradual carbon build-up deposited on our structure that develops quickly in an SEM chamber when using high electron beam currents.<sup>118</sup> The spectral agreement between the two different excitation methods should not be taken for granted. Other coupled structures have shown

CL spectra vastly different from their optical counterpart.<sup>119</sup> The localized electron beam excitation of CL selectively strengthens the plasmon resonances of the nanostructure sequentially at individual points of impact making it difficult to observe interference effects caused by strong optical fields simultaneously acting across the entire nanostructure that occurs in a plane wave excitation. The far-field spectral agreement between the optical and e-beam excitations indicates that the nanorod LSPRs are hybridized with the dipole of the side antennas but do not exhibit any interference between the respective hybridized modes. We can therefore safely decompose the spectra into three Lorentzian peaks (Figure 3.3C, lower panel) corresponding to the hybridized peaks predicted in Figure 3.2B.

Weakly excited modes can also be enhanced through the breaking of positional symmetry.<sup>120</sup> We tried to further excite higher-order nanorod LSPRs by adding a longitudinal displacement ( $\Delta x$ ) between the two side antennas along the nanorod (Figure 3.3A, right panel). The nanorod dimensions ( $420 \times 35$  nm) and square antenna length (140 nm) remained the same but we displaced one square antenna by  $\Delta x = 140$  nm, coinciding with one nanorod end, thereby aligning the poles of both square antennas to a separate pair of anti-nodes of the weakly scattering  $l = 5$  nanorod resonance. In general, the asymmetric 140 nm offset provides more clearly defined longitudinal nanorod resonances in CL maps imaged at different wavelengths (Figure 3.3B, right three panels). We also observe a wavelength dependent anti-node intensity variation where the highest photon emission occurs when the nanostructure is excited at the nanorod anti-nodes located at 0.2  $\mu\text{m}$ , 0.3  $\mu\text{m}$ , and 0.5  $\mu\text{m}$  for wavelengths 850, 700, and 650 nm, respectively. This anti-node intensity variation is caused by the positional dependence of

the side antenna coupling to the different spatial distributions of the nanorod resonances but can also be caused by fabrication irregularities. Such irregularity can be seen in the asymmetric dual-antenna configuration (Figure 3.3B, right panels) at 650 nm where the offset side antenna is closer to the nanorod towards its endpoint (0.5  $\mu\text{m}$ ) causing an increase in CL photon emission from that site.

The resonance peaks in the dark-field and CL spectra for the 140 nm offset asymmetric dual-antenna system are in good agreement while the lower energy hybrid-III peak near 850 nm is better accentuated in the CL excitation. The Lorentzian peak fits of the CL spectra (Figure 3.3C, lower panel) clearly show the identification of the three hybrid peaks with similarities to the peak fitting of the symmetric structure. Although the spectra between the two nanostructures bear resemblance, the nanorod modes,  $l = 3,4,5$ , viewed in the CL excitation maps (Figure 3.3B) do not always correspond to the hybrid spectral peak position or with the highest intensity peak at locations of peak overlapping as seen in the peak fitting (Figure 3.3C). The  $l = 5$  nanorod spatial distribution which should be more strongly associated with the hybrid-V peak is observable at 600 and 650 nm for the symmetric and asymmetric nanostructures, respectively, even though the scattering intensity of hybrid-V is lower than the overlapping hybrid-IV peak at those wavelengths. Finally, the most idyllic spatial distribution of the  $l = 3$  nanorod mode is also observed at wavelengths where the hybrid-IV peaks have higher photon emission over the hybrid-III peak. These spectral mismatches clearly demonstrate that the hybridized peaks are not exclusive to a single nanorod resonance but are truly an admixture of the different nanorod resonances that are influenced by the alignment of the poles of the side antennas with the spatial distribution of the nanorod resonances.

### 3.5. CL Imaging of Dual Antenna LDOS

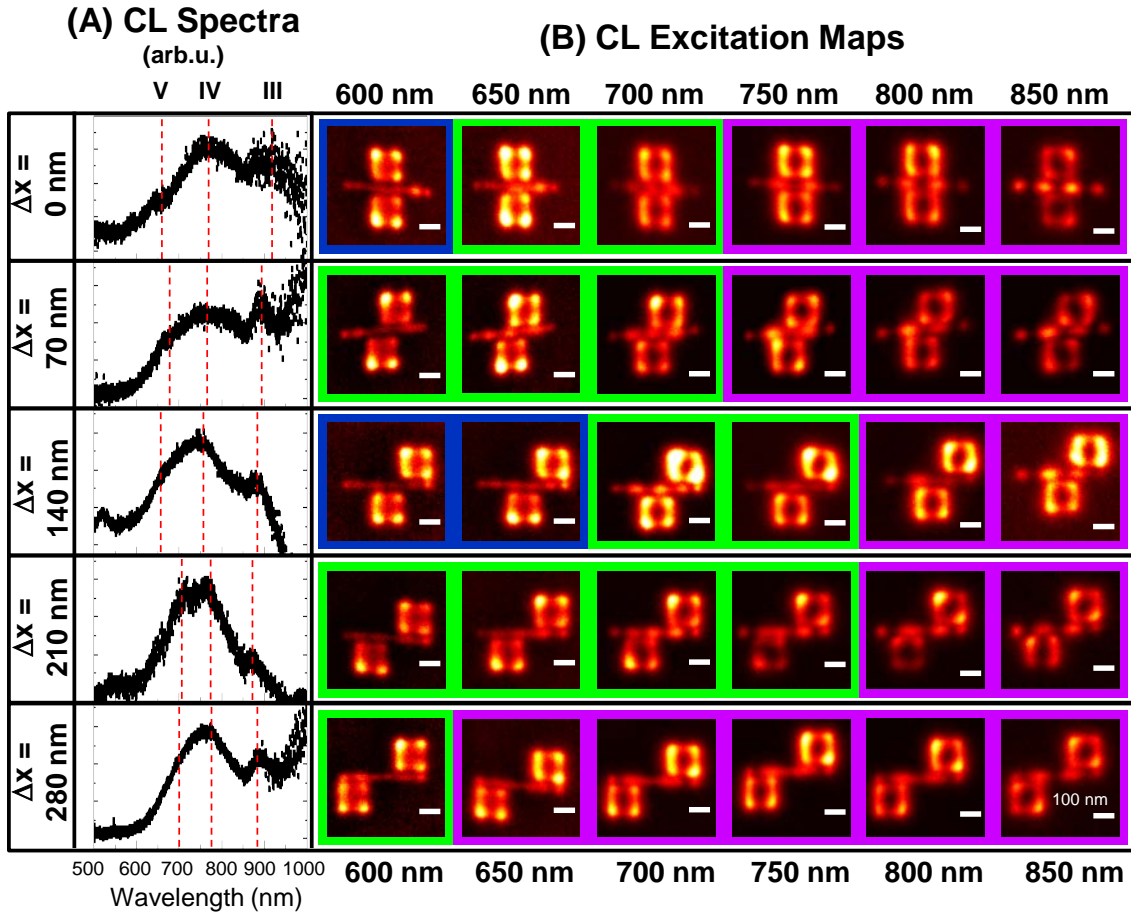


**Figure 3.4** Spectral and imaging bandwidth of dual-antenna systems. (A) CL emission intensity spectra for dual-antenna systems with different longitudinal offsets,  $\Delta x$ , between side antennas. Dashed red lines indicate three hybrid resonances (-III, -IV, -V) for each structure. (B) Bandwidth filtered (40 nm FWHM) CL excitation maps for each dual-antenna system at different wavelengths. CL image borders are colored according to the observed nanorod mode, ( $l=3$ : purple,  $l=4$ : green,  $l=5$ : blue), determined using integrated line scans through the nanorod.

To better understand how the side antenna longitudinal offset contributes to excitation bandwidth of a particular nanorod resonance we increased the longitudinal

displacement between the two side antennas in 70 nm increments on opposing sides of the center nanorod (Figure 3.4). By collecting the CL spectra (Figure 3.4A) and excitation maps across the full spectral bandwidth of the nanostructure (Figure 3.4B) we can better correlate the imaged nanorod modes to the hybridization peaks in the far-field. Each CL image was color coded by the dominant nanorod mode seen in the image and confirmed by plotting an integrated line scan through the center of the nanorod. For structures with a longitudinal displacement,  $\Delta x$ , of 140 nm or less the excitation bandwidth of the dominant mode, as determined by the wavelength filtered CL images, is between 50 and 150 nm (Figure 3.4B). These imaging bandwidths do not directly correspond with the spectral bandwidths of the hybrid peaks in the far-field spectra (Figure 3.4A). The hybridization with the side antennas and the overlapping nature of these modes allows for one nanorod mode to be the dominant mode in the CL excitation maps at wavelengths corresponding to two different hybrid peaks in the far-field. The  $l = 3$  nanorod mode (purple) is the dominant excited mode across the spectral bandwidth of the hybrid-III peak as well as a significant portion of the hybrid-IV peak for offset configurations  $\Delta x = 0, 70$  nm (Figure 3.4, top two rows). The same is also true for the  $l = 5$  mode (blue) which straddles hybrid-V and hybrid-IV peaks for  $\Delta x = 140$  nm (Figure 3.4, center row). This means that the hybridization defines the spectral features but also that the coupling strength, which is dependent on the longitudinal displacement of the side antennas, alters the weighted strength of the individual modes at a given wavelength. Near-field coupling of the side antennas to the nanorod optical cavity allows for the control of the transition wavelength between cavity modes as well as control over



the bandwidth of the dominant mode as seen from the imaging bandwidth of each individual mode in Figure 3.4B.

When the longitudinal offset between the side antennas is increased beyond 140 nm (Figure 3.4, bottom two rows) a single nanorod mode can dominate the imaging bandwidth in the CL excitation maps beyond the spectral bandwidth of any of the three hybridized peaks which individually have a spectral bandwidth no greater than 100 nm FWHM. The largest imaging bandwidth is the  $l = 3$  nanorod resonance, observed in the 280 nm offset configuration (Figure 3.4B, bottom row), that is observable in CL excitation images spans across 250 nm of our 300 nm detectable range. The hybridization diagram in Figure 3.2B gives us insight to understand how to correlate the near-field excitation images with the far-field scattering for large offset configurations. In the symmetric nanostructure ( $\Delta x = 0$  nm) described in Figure 3.2 the side antenna dimer plasmon resonance and the  $l = 3$  nanorod resonance oscillate at essentially identical energy levels resulting in a strong hybridization (i.e. large energy splitting) when these two nanostructures are brought together. The larger longitudinal offset configurations shown in Figure 3.4 ( $\Delta x = 210, 280$  nm) have side antennas that are no longer coupled together and we must treat them as individual single antennas coupling to the center nanorod. Treating the side antennas individually results in a red-shift of their LSP energies below the energy level of the  $l = 3$  nanorod mode and further away from other higher-order modes as well (Figure 3.2B). This reduced coupling to the nanorod resonances  $l = 4, 5$  and the alignment of the side antenna poles with the anti-nodes of the  $l = 3$  nanorod resonance gives the  $l = 3$  mode an extended imaging bandwidth for offset configuration  $\Delta x = 280$  nm. The far-field spectra for offset  $\Delta x = 280$  nm, is still the

result of 3 distinct but overlapping hybridized peaks but with a different bias between the three competing nanorod resonances favoring the  $l = 3$  resonance due to the positional alignment of the side antennas. Using the same nomenclature as before, hybrid-III is dominated by an admixture of the  $l = 3$  nanorod resonance with the dipolar resonance of the individual single antennas, hybrid-IV originates from the hybridization of two individual side antenna dipolar resonances and nanorod resonances  $l = 3,4$ , while hybrid-V predominately originates from the hybridization of the two individual dipolar side antennas and nanorod resonances  $l = 4,5$ .

The offset configuration  $\Delta x = 210$  nm shows a preferential alignment towards exciting the  $l = 4$  nanorod mode (Figure 3.4B). Although the side antennas are spatially decoupled from one another and the individual dipolar side antenna resonances have shifted to lower energies away from nanorod resonances  $l = 4,5$ , this configuration still preferentially excites the  $l = 4$  nanorod mode due to the strong positional alignment with the poles of the side antenna dipole mode.

The control over the far-field spectrum through the engineered antenna-nanorod coupling is supported by the FDTD calculations. The spectral shifts for each hybridized mode also vary when altering the side antennas offset. Both the hybrid-III and hybrid-IV peaks undergo noticeable spectral shifts ( $\Delta\lambda \sim 50$  nm), but the shift is larger for hybrid-V ( $\Delta\lambda \sim 80$  nm). The hybrid-V shift to higher energies coincides with the observation of the  $l = 5$  mode in the excitation maps and reflects greater spectral separation from the other hybridized modes. Smaller antennas were used to excite  $l > 5$  LSPRs, but those higher energy modes were damped by the proximity to the interband transitions in Au and limited by the spatial resolution of our CL system.

The side nanoantenna coupling also leads to unique intensity near-field profiles for the nanorod LSPRs that differ from an isolated nanorod as well as from expected Fabry-Pérot standing waves. Since the radiation decay of a point-source emitter (electron) is directly proportional to nearby cavity modes<sup>97</sup> CL imaging represents one of the few methods capable of measuring the spatial and intensity distribution of these optical modes without distortion.<sup>54,89,90,97,105,121</sup> In Figure 3.4B, the  $l = 3$  nanorod mode (purple) at 850 nm for the symmetric configuration ( $\Delta x = 0$  nm) closely resembles the same resonance for the isolated nanorod in Figure 3.1C. However, breaking the symmetry ( $\Delta x = 70$  nm) at 850 nm causes the relative intensity between the anti-nodes to become skewed to the left center anti-node. The anti-node intensity variation along the nanorod LSPR is the result of modifying the LDOS of the nanorod through plasmon hybridization<sup>91</sup> and is not accounted for in simple cavity models. Anti-node intensity variation can be seen in most offset configurations at some point along the CL imaging spectrum and is the direct result of plasmon mode hybridization through the placement of the side antennas at various positions adjacent to the longitudinal axis of the nanorod.

A spatial variation in the nanorod modes also occurs through plasmon coupling with the side nanoantennas. We observe a greater spatial distortion of the nanorod optical cavity modes for resonances with wider imaging bandwidth (Figure 3.4B), where the center anti-nodes of a given mode are either stretched apart at shorter excitation wavelengths or compressed together at longer wavelengths. To track the spatial distortion of the nanorod modes we measure the half-wavelength of the LSP,  $\lambda_{sp}/2$ , determined by the distance between the maxima of any two adjacent nodes or anti-nodes in the CL excitation maps (Figure 3.1C). In the dual-antenna systems, for a given nanorod mode, as

the  $\lambda_{sp}$  and distance between the center anti-nodes increases (shorter wavelengths), the center anti-nodes spread apart exacerbating previously observed “ $\lambda_{sp}$ -compression”,<sup>105</sup> or “anti-node bunching”,<sup>108</sup> at the terminal ends. At longer wavelengths, the center anti-nodes compress together (i.e. distance between the center anti-nodes decreases), thus causing  $\lambda_{sp}$  values to decrease in the middle of the nanorod while increasing at the endpoints in direct contrast to observations of isolated nanorods. This anti-node “drift” along the nanorod is primarily caused by the near-field interaction with the side antennas and should not be confused by the normally observed “anti-node bunching” caused by the phase shift due to reflections at nanorod ends for isolated nanorods.<sup>105,107,108</sup> Particularly interesting is the CL imaging progression (for increasing wavelengths) of the  $\Delta x = 210$  nm dual-antenna configuration that shows  $\lambda_{sp}$ -compression of the central anti-nodes, instead of at the nanorod ends. The left central anti-nodes of the  $l = 4$  resonance (the 2<sup>nd</sup> and 3<sup>rd</sup> anti-nodes from the left at 750 nm) merge to become a single anti-node of the  $l = 3$  resonance at 800 nm. This is a counter-intuitive result as increasing wavelengths should show a gradual increase in the distance between the anti-nodes and overall  $\lambda_{sp}$ ,<sup>52,57,105</sup> but plasmon hybridization alters the behavior of the spatial distribution of individual nanorod modes.

### 3.6. Modifying Nanorod LDOS

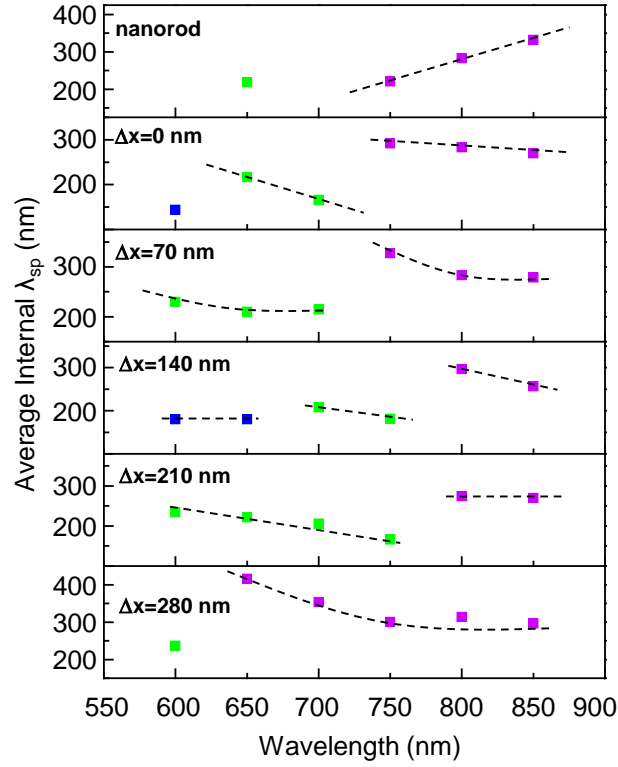


**Figure 3.5** Mode compression/relaxation behavior for isolated nanorod and dual-antenna systems. The LSPR wavelength,  $\lambda_{sp}$ , calculated by averaging the distances between internal anti-nodes of nanorod resonances are plotted as a function of excitation wavelength for each system. Data points are colored according to nanorod mode excited ( $l=3$ : purple,  $l=4$ : green,  $l=5$ : blue). Dashed lines are used to highlight  $\lambda_{sp}$  trends within a given nanorod mode.

To more generally quantify the spatial distortion of the nanorod modes across the spectrum we plotted the average internal  $\lambda_{sp}$  for each dual-antenna configuration and for a single nanorod as a function of excitation wavelength (Figure 3.5). Integrated line profiles through the nanorod center were taken of the CL images for the different dual-

antenna systems (Figure 3.4B) and for an isolated nanorod (Figure 3.1B and 3.1C) at 50 nm increments across the visible spectral bandwidth.  $\lambda_{sp}$  was calculated using the distance between only the internal anti-nodes (i.e. excluding the terminal anti-nodes) to eliminate variations caused by the reflections at the nanorod ends.<sup>57,105</sup> The data points are colored according to the excited nanorod mode and are color correlated to the corresponding CL maps in Figure 3.4B. We can clearly see large compressive trends ( $\Delta\lambda_{sp} \geq 150$  nm) of the internal anti-nodes at longer wavelengths for the  $l = 3$  and  $l = 4$  LSPRs in the antenna offset configurations  $\Delta y = 280$  and  $210$  nm, respectively. We can also see similar trends for smaller antenna offsets ( $\Delta x \leq 140$  nm), where the  $\lambda_{sp}$  decreases slightly (internal anti-node compression) at increasing wavelengths for a given LSPR until the onset of a new lower order mode causes the  $\lambda_{sp}$  to abruptly increase. This staircase pattern for  $\lambda_{sp}$  values continues for all LSPRs influenced by the interaction with the side nanoantennas. Although the overall increasing progression of the  $\lambda_{sp}$  at longer wavelengths (i.e. lower order modes) is seen in both coupled and uncoupled systems alike the  $\lambda_{sp}$  within a given nanorod mode expands at longer wavelengths for an uncoupled nanorod (Figure 3.5, upper panel) in direct contrast to coupled systems and unaccounted for in 1-D Fabry-Pérot models. This change in anti-node positioning along a nanorod shows that the behavior of the LDOS of plasmonic optical cavities can be altered and controlled by near-field coupling of shorter dipole antennas.

### 3.7. Conclusions

In conclusion, we demonstrated the enhancement of the scattering strength of weak higher-order nanorod resonances through near-field coupling with nanoantennas. Strong coupling responsible for the enhancement is the result of energy overlap and the positional alignment between the nanorod LSPRs and the dipole moment of the adjacent nanoantennas. The simple dual-antenna design allowed us to easily compare both optical and electron spectroscopy techniques to better understand mode hybridization in such coupled nanostructures. CL imaging revealed that anti-nodes of uncoupled nanorod resonances do not remain in stationary positions throughout its spectral bandwidth as expected from eigenmode solutions of nanorod resonances. Instead the anti-nodes of the nanorod LSPRs are shown to “drift” between stationary positions as a function of wavelength. Near-field coupling to nanoantennas can control the behavior of anti-node “drift” directly affecting the spectral bandwidth of a given mode. The hybridization of the multipolar nanorod resonances with the nanoantenna dipoles not only enhanced the far-field power of these resonances but also alters the near-field intensities, spatial distribution behavior, and spectral bandwidth of individual plasmonic modes. Near-field coupling of nanoantennas to nanorod optical cavities shows that plasmon hybridization is a powerful method for controlling the radiative LDOS which will allow for better design, engineering, and control of the electromagnetic response of future optical antennas.

## Chapter 4

# Conclusions and Future Directions

This thesis covers the basis of utilizing optical (light scattering) and e-beam (cathodoluminescence) far-field spectroscopies for investigating the longitudinal resonances of Au nanorod nanostructures. A coupled dual-antenna structure provides a simple system to better investigate the optical activation and enhancement of different higher order nanorod resonances with plane wave excitation, near-field coupling or fast electron impact. A qualitative agreement between the radiative spectra produced for both the optical and electron excitation for different dual antenna systems has been shown in this thesis. The experimental spectroscopic agreement between these two excitation methods makes this system ideal for developing better theoretical models to provide a more quantitative agreement between electron and optical based excitations which has only recently been considered.

The quantitative differences between photon and electron excitations (CL, EELS) are not easily relatable but establishing a firmer relationship between these two methods would help to translate the characterization from EELS and CL into predictive scattering properties of nanoantennas that are of greater technological importance. Modal decomposition of LDOS and near-field scanning microscope (NSOM) signals into geometric modes has provided an initial basis for comparing electron based EELS and photon based NSOM results. Light scattering for spheres has also been decomposed and rewritten into an expression with distinct weighting factors directly comparable to EELS probability. To further test these results a weighting factor could be assigned for each of



the side antennas in the dual antenna design in this thesis. The weighting factor would need to depend on the position and coupling strength of the side antennas. The side antennas could be viewed as secondary sources of electron excitation and given their own modified impact parameter relative to the one used for the primary electron incident on the nanorod.

If the side antennas can be incorporated into a modal decomposition of plane wave excitations then researchers could better consider the scenario between antenna dimers of different materials. If the side antennas can mimic a secondary source of electron excitation could they also mimic the activation of bulk modes in lower energy ultra-small quantum plasmonic systems recently investigated?

Other possible directions based on this work would be using chemically fabricated center nanorods instead of the poly-crystalline nanorods made from e-beam evaporation. Single crystalline nanorods would reduce the loss in fragile higher-order modes allowing them to more effectively couple to the side antennas. Investigating the changes in the LDOS of the nanorod based on the thickness of the center nanorod will also better examine the dependence of the lateral dimension of the nanorod to the strength of higher order modes throughout the nanorod in contrast to a local inducement of charge near the side antennas that does not manifest across the entire center nanorod.

## References

1. Gobin, A. M. *et al.* Near-infrared resonant nanoshells for combined optical imaging and photothermal cancer therapy. *Nano Lett.* **7**, 1929-1934 (2007).
2. Huschka, R. *et al.* Gene Silencing by Gold Nanoshell-Mediated Delivery and Laser-Triggered Release of Antisense Oligonucleotide and siRNA. *ACS Nano* **6**, 7681-7691 (2012).
3. Bardhan, R., Lal, S., Joshi, A. & Halas, N. J. Theranostic Nanoshells: From Probe Design to Imaging and Treatment of Cancer. *Accounts of Chemical Research* **44**, 936-946 (2011).
4. Pendry, J. B., Schurig, D. & Smith, D. R. Controlling Electromagnetic Fields. *Science* **312**, 1780-1782 (2006).
5. Edwards, B., Alù, A., Silveirinha, M. G. & Engheta, N. Experimental Verification of Plasmonic Cloaking at Microwave Frequencies with Metamaterials. *Physical Review Letters* **103**, 153901 (2009).
6. Zhang, S., Genov, D. A., Wang, Y., Liu, M. & Zhang, X. Plasmon-Induced Transparency in Metamaterials. *Physical Review Letters* **101**, 047401 (2008).
7. Xiao, S. *et al.* Loss-free and active optical negative-index metamaterials. *Nature* **466**, 735-738 (2010).
8. Knight, M. W., Sobhani, H., Nordlander, P. & Halas, N. J. Photodetection with Active Optical Antennas. *Science* **332**, 702-704 (2011).
9. Sobhani, A. *et al.* Narrowband photodetection in the near-infrared with a plasmon-induced hot electron device. *Nat Commun* **4**, 1643 (2013).
10. Mukherjee, S. *et al.* Hot Electrons Do the Impossible: Plasmon-Induced Dissociation of H<sub>2</sub> on Au. *Nano Letters* **13**, 240-247 (2012).
11. Liu, Z., Hou, W., Pavaskar, P., Aykol, M. & Cronin, S. B. Plasmon Resonant Enhancement of Photocatalytic Water Splitting Under Visible Illumination. *Nano Letters* **11**, 1111-1116 (2011).
12. Jin, Y. & Gao, X. Plasmonic fluorescent quantum dots. *Nat Nano* **4**, 571-576 (2009).
13. Tan, S. F. *et al.* Quantum Plasmon Resonances Controlled by Molecular Tunnel Junctions. *Science* **343**, 1496-1499 (2014).

14. Zuloaga, J., Prodan, E. & Nordlander, P. Quantum Description of the Plasmon Resonances of a Nanoparticle Dimer. *Nano Letters* **9**, 887-891 (2009).
15. Manjavacas, A. & García de Abajo, F. J. Tunable plasmons in atomically thin gold nanodisks. *Nat Commun* **5** (2014).
16. Betzig, E. & Chichester, R. J. Single Molecules Observed by Near-Field Scanning Optical Microscopy. *Science* **262**, 1422-1425 (1993).
17. Dürig, U., Pohl, D. W. & Rohner, F. Near-field optical-scanning microscopy. *Journal of Applied Physics* **59**, 3318-3327 (1986).
18. Folling, J. *et al.* Fluorescence nanoscopy by ground-state depletion and single-molecule return. *Nat Meth* **5**, 943-945 (2008).
19. Rust, M. J., Bates, M. & Zhuang, X. Sub-diffraction-limit imaging by stochastic optical reconstruction microscopy (STORM). *Nat Meth* **3**, 793-796 (2006).
20. Zhuang, X. Nano-imaging with STORM. *Nat Photon* **3**, 365-367 (2009).
21. Novotny, L. & van Hulst, N. Antennas for light. *Nat. Photonics* **5**, 83-90 (2011).
22. Nie, S. & Emory, S. R. Probing Single Molecules and Single Nanoparticles by Surface-Enhanced Raman Scattering. *Science* **275**, 1102-1106 (1997).
23. Kneipp, K. *et al.* Single Molecule Detection Using Surface-Enhanced Raman Scattering (SERS). *Physical Review Letters* **78**, 1667-1670 (1997).
24. Tam, F., Goodrich, G. P., Johnson, B. R. & Halas, N. J. Plasmonic Enhancement of Molecular Fluorescence. *Nano Letters* **7**, 496-501 (2007).
25. Anger, P., Bharadwaj, P. & Novotny, L. Enhancement and Quenching of Single-Molecule Fluorescence. *Physical Review Letters* **96**, 113002 (2006).
26. Bardhan, R., Grady, N. K., Cole, J. R., Joshi, A. & Halas, N. J. Fluorescence Enhancement by Au Nanostructures: Nanoshells and Nanorods. *ACS Nano* **3**, 744-752 (2009).
27. Bharadwaj, P. & Novotny, L. Spectral dependence of single molecule fluorescence enhancement. *Opt. Express* **15**, 14266-14274 (2007).
28. Taminiau, T. H., Moerland, R. J., Segerink, F. B., Kuipers, L. & van Hulst, N. F.  $\lambda/4$  Resonance of an optical monopole antenna probed by single molecule fluorescence. *Nano Lett.* **7**, 28-33 (2007).
29. Taminiau, T. H., Stefani, F. D., Segerink, F. B. & van Hulst, N. F. Optical antennas direct single-molecule emission. *Nat. Photonics* **2**, 234-237 (2008).

30. Zijlstra, P., Paulo, P. M. R. & Orrit, M. Optical detection of single non-absorbing molecules using the surface plasmon resonance of a gold nanorod. *Nat. Nanotechnol.* **7**, 379-382 (2012).
31. Lakowicz, J. R., Malicka, J., Gryczynski, I. & Gryczynski, Z. Directional surface plasmon-coupled emission: a new method for high sensitivity detection. *Biochemical and Biophysical Research Communications* **307**, 435-439 (2003).
32. Brönstrup, G. *et al.* Optical Properties of Individual Silicon Nanowires for Photonic Devices. *ACS Nano* **4**, 7113-7122 (2010).
33. Kempa, K. *et al.* Carbon Nanotubes as Optical Antennae. *Adv Mater* **19**, 421-426 (2007).
34. Mühlischlegel, P., Eisler, H.-J., Martin, O. J. F., Hecht, B. & Pohl, D. W. Resonant Optical Antennas. *Science* **308**, 1607-1609 (2005).
35. Kreibig, U. & Vollmer, M. *Optical properties of metal clusters*. (Springer, 1995).
36. Barnes, W. L., Dereux, A. & Ebbesen, T. W. Surface plasmon subwavelength optics. *Nature* **424**, 824-830 (2003).
37. Prodan, E., Radloff, C., Halas, N. J. & Nordlander, P. A Hybridization Model for the Plasmon Response of Complex Nanostructures. *Science* **302**, 419-422 (2003).
38. Bohren, C. F. & Huffman, D. R. *Absorption and scattering of light by small particles*. (Wiley, 1983).
39. Neumann, O. *et al.* Solar Vapor Generation Enabled by Nanoparticles. *ACS Nano* **7**, 42-49 (2012).
40. Linic, S., Christopher, P. & Ingram, D. B. Plasmonic-metal nanostructures for efficient conversion of solar to chemical energy. *Nat Mater* **10**, 911-921 (2011).
41. Stuart, H. R. & Hall, D. G. Absorption enhancement in silicon-on-insulator waveguides using metal island films. *Applied Physics Letters* **69**, 2327-2329 (1996).
42. Knight, M. W. *et al.* Nanoparticle-mediated coupling of light into a nanowire. *Nano Lett.* **7**, 2346-2350 (2007).
43. Zhang, S. & Xu, H. Optimizing Substrate-Mediated Plasmon Coupling toward High-Performance Plasmonic Nanowire Waveguides. *ACS Nano* **6**, 8128-8135 (2012).

44. Day, J. K., Neumann, O., Grady, N. K. & Halas, N. J. Nanostructure-Mediated Launching and Detection of 2D Surface Plasmons. *ACS Nano* **4**, 7566-7572 (2010).
45. Lal, S., Hafner, J. H., Halas, N. J., Link, S. & Nordlander, P. Noble Metal Nanowires: From Plasmon Waveguides to Passive and Active Devices. *Acc. Chem. Res.* **45**, 1887-1895 (2012).
46. Wang, H., Brandl, D. W., Nordlander, P. & Halas, N. J. Plasmonic Nanostructures: Artificial Molecules. *Accounts of Chemical Research* **40**, 53-62 (2006).
47. Novotny, L. & Hecht, B. (Cambridge University Press, Cambridge, 2012).
48. Imura, K., Nagahara, T. & Okamoto, H. Plasmon Mode Imaging of Single Gold Nanorods. *Journal of the American Chemical Society* **126**, 12730-12731 (2004).
49. Wei, H., Zhang, S., Tian, X. & Xu, H. Highly tunable propagating surface plasmons on supported silver nanowires. *Proc. Natl. Acad. Sci. U. S. A.* **110**, 4494-4499 (2013).
50. Mie, G. Beiträge zur Optik trüber Medien, speziell kolloidaler Metallösungen. *Ann Phys-Berlin* **330**, 377-445 (1908).
51. Maier, S. A. *Plasmonics: Fundamentals and Applications: Fundamentals and Applications*. (Springer, 2007).
52. Schider, G. *et al.* Plasmon dispersion relation of Au and Ag nanowires. *Phys. Rev. B* **68**, 155427 (2003).
53. Dorfmueller, J. *et al.* Fabry-Pérot Resonances in One-Dimensional Plasmonic Nanostructures. *Nano Lett.* **9**, 2372-2377 (2009).
54. Douillard, L. *et al.* Short Range Plasmon Resonators Probed by Photoemission Electron Microscopy. *Nano Lett.* **8**, 935-940 (2008).
55. Taminiau, T. H., Stefani, F. D. & van Hulst, N. F. Optical Nanorod Antennas Modeled as Cavities for Dipolar Emitters: Evolution of Sub- and Super-Radiant Modes. *Nano Lett.* **11**, 1020-1024 (2011).
56. Okamoto, H. & Imura, K. Near-field imaging of optical field and plasmon wavefunctions in metal nanoparticles. *Journal of Materials Chemistry* **16**, 3920-3928 (2006).
57. Coenen, T., Vesseur, E. J. R. & Polman, A. Deep Subwavelength Spatial Characterization of Angular Emission from Single-Crystal Au Plasmonic Ridge Nanoantennas. *ACS Nano* **6**, 1742-1750 (2012).

58. Novotny, L. Effective Wavelength Scaling for Optical Antennas. *Phys. Rev. Lett.* **98**, 266802 (2007).
59. Jin, J. *The Finite Element Method in Electromagnetics*. 2 edn. (Wiley-IEEE Press, 2002).
60. Taflove, A. & Hagness, S. C. *Computational Electrodynamics: The Finite-difference Time Domain Method*. (Artech House, 2000).
61. Bryant, G. W., García de Abajo, F. J. & Aizpurua, J. Mapping the Plasmon Resonances of Metallic Nanoantennas. *Nano Letters* **8**, 631-636 (2008).
62. Jana, N. R., Gearheart, L. & Murphy, C. J. Wet Chemical Synthesis of High Aspect Ratio Cylindrical Gold Nanorods. *The Journal of Physical Chemistry B* **105**, 4065-4067 (2001).
63. Nikoobakht, B. & El-Sayed, M. A. Preparation and Growth Mechanism of Gold Nanorods (NRs) Using Seed-Mediated Growth Method. *Chemistry of Materials* **15**, 1957-1962 (2003).
64. Sau, T. K. & Murphy, C. J. Room Temperature, High-Yield Synthesis of Multiple Shapes of Gold Nanoparticles in Aqueous Solution. *Journal of the American Chemical Society* **126**, 8648-8649 (2004).
65. Nakashima, H., Furukawa, K., Kashimura, Y. & Torimitsu, K. Self-Assembly of Gold Nanorods Induced by Intermolecular Interactions of Surface-Anchored Lipids. *Langmuir* **24**, 5654-5658 (2008).
66. Yang, S.-M., Jang, S. G., Choi, D.-G., Kim, S. & Yu, H. K. Nanomachining by Colloidal Lithography. *Small* **2**, 458-475 (2006).
67. Gates, B. D. *et al.* New Approaches to Nanofabrication: Molding, Printing, and Other Techniques. *Chemical Reviews* **105**, 1171-1196 (2005).
68. Vieu, C. *et al.* Electron beam lithography: resolution limits and applications. *Applied Surface Science* **164**, 111-117 (2000).
69. Nonogaki, S., Takumi, U. & Ito, T. *Microlithography Fundamentals in Semiconductor Devices and Fabrication Technology*. (Taylor & Francis, 1998).
70. Ditlbacher, H. *et al.* Silver Nanowires as Surface Plasmon Resonators. *Physical Review Letters* **95**, 257403 (2005).
71. Söennichsen, C. *Plasmons in metal nanostructures* Ph.D. thesis, Ludwig-Maximilians-Universität, (2001).

72. Murphy, D. B. *Fundamentals of Light Microscopy and Electronic Imaging*, (Wiley, 2001).
73. Verebes, G. S. *et al.* Hyperspectral enhanced dark field microscopy for imaging blood cells. *Journal of Biophotonics* **6**, 960-967 (2013).
74. Sönnichsen, C. *et al.* Spectroscopy of single metallic nanoparticles using total internal reflection microscopy. *Applied Physics Letters* **77**, 2949-2951 (2000).
75. Mukherjee, S. *et al.* Fanoshells: Nanoparticles with Built-in Fano Resonances. *Nano Letters* **10**, 2694-2701 (2010).
76. Clark, A. W., Glidle, A., Cumming, D. R. S. & Cooper, J. M. Plasmonic Split-Ring Resonators as Dichroic Nanophotonic DNA Biosensors. *Journal of the American Chemical Society* **131**, 17615-17619 (2009).
77. Pors, A., Willatzen, M., Albrechtsen, O. & Bozhevolnyi, S. I. From plasmonic nanoantennas to split-ring resonators: tuning scattering strength. *J. Opt. Soc. Am. B* **27**, 1680-1687 (2010).
78. Fischer, H. & Martin, O. J. F. Engineering the optical response of plasmonic nanoantennas. *Optics Express* **16**, 9144-9154 (2008).
79. Kinkhabwala, A. *et al.* Large single-molecule fluorescence enhancements produced by a bowtie nanoantenna. *Nat Photon* **3**, 654-657 (2009).
80. Hao, F. & Nordlander, P. Plasmonic coupling between a metallic nanosphere and a thin metallic wire. *Appl. Phys. Lett.* **89**, 103101 (2006).
81. Le, F. *et al.* Plasmons in the metallic nanoparticle - Film system as a tunable impurity problem. *Nano Lett.* **5**, 2009-2013 (2005).
82. Slaughter, L. S., Wu, Y., Willingham, B. A., Nordlander, P. & Link, S. Effects of Symmetry Breaking and Conductive Contact on the Plasmon Coupling in Gold Nanorod Dimers. *ACS Nano* **4**, 4657-4666 (2010).
83. Willingham, B., Brandl, D. W. & Nordlander, P. Plasmon hybridization in nanorod dimers. *Appl. Phys. B* **93**, 209-216 (2008).
84. Funston, A. M., Novo, C., Davis, T. J. & Mulvaney, P. Plasmon Coupling of Gold Nanorods at Short Distances and in Different Geometries. *Nano Letters* **9**, 1651-1658 (2009).
85. Ritchie, R. H. Plasma Losses by Fast Electrons in Thin Films. *Physical Review* **106**, 874-881 (1957).

86. Pines, D. Collective Energy Losses in Solids. *Reviews of Modern Physics* **28**, 184-198 (1956).
87. Powell, C. J. & Swan, J. B. Origin of the Characteristic Electron Energy Losses in Aluminum. *Physical Review* **115**, 869-875 (1959).
88. Teng, Y.-Y. & Stern, E. A. Plasma Radiation from Metal Grating Surfaces. *Physical Review Letters* **19**, 511-514 (1967).
89. Kuttge, M. *et al.* Local density of states, spectrum, and far-field interference of surface plasmon polaritons probed by cathodoluminescence. *Phys. Rev. B* **79**, 113405 (2009).
90. Vesseur, E. J. R. *et al.* Plasmonic excitation and manipulation with an electron beam. *MRS Bull.* **37**, 752-760 (2012).
91. Viarbitskaya, S. *et al.* Tailoring and imaging the plasmonic local density of states in crystalline nanoprisms. *Nat. Mater.* **12**, 426-432 (2013).
92. García de Abajo, F. J. Optical excitations in electron microscopy. *Reviews of Modern Physics* **82**, 209-275 (2010).
93. Coenen, T., Bernal Arango, F., Femius Koenderink, A. & Polman, A. Directional emission from a single plasmonic scatterer. *Nat Commun* **5** (2014).
94. Sapienza, R. *et al.* Deep-subwavelength imaging of the modal dispersion of light. *Nat. Mater.* **11**, 781-787 (2012).
95. Weeber, J.-C., Dereux, A., Girard, C., Krenn, J. R. & Goudonnet, J.-P. Plasmon polaritons of metallic nanowires for controlling submicron propagation of light. *Phys. Rev. B* **60**, 9061-9068 (1999).
96. Imura, K., Nagahara, T. & Okamoto, H. Near-field optical imaging of plasmon modes in gold nanorods. *J. Chem. Phys.* **122**, 154701 (2005).
97. García de Abajo, F. J. & Kociak, M. Probing the Photonic Local Density of States with Electron Energy Loss Spectroscopy. *Phys. Rev. Lett.* **100**, 106804 (2008).
98. Anker, J. N. *et al.* Biosensing with plasmonic nanosensors. *Nat. Mater.* **7**, 442-453 (2008).
99. Billot, L. *et al.* Surface enhanced Raman scattering on gold nanowire arrays: Evidence of strong multipolar surface plasmon resonance enhancement. *Chem. Phys. Lett.* **422**, 303-307 (2006).



100. Yan, R., Pausauskie, P., Huang, J. & Yang, P. Direct photonic–plasmonic coupling and routing in single nanowires. *Proc. Natl. Acad. Sci. U. S. A.* **106**, 21045-21050 (2009).
101. Large, N., Abb, M., Aizpurua, J. & Muskens, O. L. Photoconductively loaded plasmonic nanoantenna as building block for ultracompact optical switches. *Nano Letters* **10**, 1741-1746 (2010).
102. Gao, C., Zhang, Q., Lu, Z. & Yin, Y. Templated Synthesis of Metal Nanorods in Silica Nanotubes. *Journal of the American Chemical Society* **133**, 19706-19709 (2011).
103. Barnard, E. S., White, J. S., Chandran, A. & Brongersma, M. L. Spectral properties of plasmonic resonator antennas. *Opt. Express* **16**, 16529-16537 (2008).
104. Gómez-Medina, R., Yamamoto, N., Nakano, M. & Abajo, F. J. G. d. Mapping plasmons in nanoantennas via cathodoluminescence. *New J. Phys.* **10**, 105009 (2008).
105. Nicoletti, O. *et al.* Surface plasmon modes of a single silver nanorod: an electron energy loss study. *Opt. Express* **19**, 15371-15379 (2011).
106. Zhang, S., Chen, L., Huang, Y. & Xu, H. Reduced linewidth multipolar plasmon resonances in metal nanorods and related applications. *Nanoscale* **5**, 6985-6991 (2013).
107. Alber, I. *et al.* Visualization of Multipolar Longitudinal and Transversal Surface Plasmon Modes in Nanowire Dimers. *ACS Nano* **5**, 9845-9853 (2011).
108. Rossouw, D., Couillard, M., Vickery, J., Kumacheva, E. & Botton, G. A. Multipolar Plasmonic Resonances in Silver Nanowire Antennas Imaged with a Subnanometer Electron Probe. *Nano Lett.* **11**, 1499-1504 (2011).
109. Huschka, R. *et al.* Light-Induced Release of DNA from Gold Nanoparticles: Nanoshells and Nanorods. *Journal of the American Chemical Society* **133**, 12247-12255 (2011).
110. Ye, X. *et al.* Improved Size-Tunable Synthesis of Monodisperse Gold Nanorods through the Use of Aromatic Additives. *ACS Nano* **6**, 2804-2817 (2012).
111. Curto, A. G. *et al.* Multipolar radiation of quantum emitters with nanowire optical antennas. *Nat. Commun.* **4**, 1750 (2013).
112. Nordlander, P., Oubre, C., Prodan, E., Li, K. & Stockman, M. I. Plasmon Hybridization in Nanoparticle Dimers. *Nano Lett.* **4**, 899-903 (2004).

113. Johnson, P. B. & Christy, R. W. Optical-Constants of Noble-Metals. *Phys. Rev. B* **6**, 4370-4379 (1972).
114. Palik, E. D. *Handbook of Optical Constants of Solids*. Vol. 1 804 (Academic Press, 1985).
115. Knight, M. W. *et al.* Aluminum Plasmonic Nanoantennas. *Nano Lett.* **12**, 6000-6004 (2012).
116. Vesseur, E. J. R., de Waele, R., Kuttge, M. & Polman, A. Direct Observation of Plasmonic Modes in Au Nanowires Using High-Resolution Cathodoluminescence Spectroscopy. *Nano Lett.* **7**, 2843-2846 (2007).
117. Krenn, J. R. *et al.* Design of multipolar plasmon excitations in silver nanoparticles. *Appl. Phys. Lett.* **77**, 3379-3381 (2000).
118. Song, M., des Francs, G. C. & Bouhelier, A. Influence of an Electron Beam Exposure on the Surface Plasmon Resonance of Gold Nanoparticles. *Plasmonics* **9**, 343-348 (2014).
119. Lassiter, J. B. *et al.* Designing and Deconstructing the Fano Lineshape in Plasmonic Nanoclusters. *Nano Lett.* **12**, 1058-1062 (2011).
120. Bigelow, N. W., Vashillo, A., Camden, J. P. & Masiello, D. J. Signatures of Fano Interferences in the Electron Energy Loss Spectroscopy and Cathodoluminescence of Symmetry-Broken Nanorod Dimers. *ACS Nano* **7**, 4511-4519 (2013).
121. Vesseur, E. J. R., García de Abajo, F. J. & Polman, A. Modal Decomposition of Surface-Plasmon Whispering Gallery Resonators. *Nano Lett.* **9**, 3147-3150 (2009).